



# **Stability and degradation mechanisms in organic solar cells**

Von der Fakultät für Mathematik und Naturwissenschaften der Carl von Ossietzky  
Universität Oldenburg zur Erlangung des Grades und Titels eines  
Doktors der Naturwissenschaften (Dr. rer. nat.)  
angenommene Dissertation

von

**Bernhard Ecker**

geboren am 3. August 1983 in Landshut



Erstgutachter: Prof. Dr. Jürgen Parisi

Zweitgutachter: Prof. Dr. Elizabeth von Hauff; Prof. Dr. Carsten Agert

Tag der Disputation: 26. April 2012

## **Abstract**

This thesis deals with stability improvements and the investigation of degradation mechanisms in organic solar cells. Organic solar cells have been in the focus of extensive academic research for over almost two decades and are currently entering the market in small scale applications. For successful large scale applications, next to the improvement of the power conversion efficiency, the stability of organic solar cells has to be increased. This thesis is dedicated to the investigation of novel materials and architectures to study stability-related issues and degradation mechanisms in order to contribute to the basic understanding of the working principles of organic solar cells. Here, impedance spectroscopy, a frequency domain technique, is used to gain information about stability and degradation mechanisms in organic solar cells. In combination with systematic variations in the preparation of solar cells, impedance spectroscopy gives the possibility to differentiate between interface and bulk dominated effects. Additionally, impedance spectroscopy gives access to the dielectric properties of the device, such as capacitance. This offers among other things the opportunity to probe the charge carrier concentration and the density of states. Another powerful way of evaluation is the combination of experimentally obtained impedance spectra with equivalent circuit modelling. The thesis presents results on novel materials and solar cell architectures for efficient hole and electron extraction. This indicates the importance of knowledge over interlayers and interfaces for improving both the efficiency and stability of organic solar cells.

## **Zusammenfassung**

Die vorliegende Dissertation beschäftigt sich mit der Untersuchung von Maßnahmen zur Erhöhung der Stabilität, sowie mit Degradationsmechanismen in organischen Solarzellen. Organische Solarzellen sind seit über zwei Jahrzehnten im Fokus intensiver Forschung und zudem in ersten Anwendungen auf dem Markt zu finden. Für den weiteren Erfolg, vor allem von großflächigen Anwendungen, ist es neben der weiteren Verbesserung des Wirkungsgrades von großer Bedeutung, die Stabilität und Lebensdauer organischer Solarzellen zu erhöhen. Folglich beschäftigt sich diese Dissertation mit der Untersuchung neuartiger Materialien und Solarzellenarchitekturen, um zum Verständnis grundlegender Prozesse in organischen Solarzellen, besonders hinsichtlich der Stabilität, beizutragen. Dazu wird die Impedanzspektroskopie, eine Untersuchungsmethode, die in der Frequenzdomäne arbeitet, eingesetzt. In Kombination mit systematischen Variationen in der Solarzellenpräparation erlaubt sie die Unterscheidung von Volumen- und Grenzflächeneffekten. Zusätzlich können mittels Impedanzspektroskopie die dielektrischen Eigenschaften, wie zum Beispiel die Kapazität, von Solarzellen bestimmt werden. Dies erlaubt unter anderem die Bestimmung der Ladungsträgerkonzentration und der Zustandsdichte. Weiterhin gibt die Impedanzspektroskopie in Kombination mit Ersatzschaltbildanalysen zusätzliche Einblicke in interne Solarzellenprozesse. In der vorliegenden Dissertation werden neuartige Materialien und Solarzellenarchitekturen für die effiziente Extraktion von Ladungsträgern aus der Solarzelle untersucht. Sie zeigt damit die Bedeutung von Zwischenschichten und Grenzflächen für die Effizienz und Stabilität organischer Solarzellen.



# Contents

<b>Abstract .....</b>	<b>4</b>
<b>Zusammenfassung .....</b>	<b>5</b>
<b>1 Introduction.....</b>	<b>9</b>
<b>2 Fundamentals of organic photovoltaics and impedance spectroscopy ....</b>	<b>12</b>
2.1 Organic semiconductors .....	12
2.2 Organic photovoltaics .....	16
2.2.1 Elementary processes in organic solar cells.....	17
2.2.2 The bulk-heterojunction concept .....	18
2.3 Degradation mechanisms in organic solar cells.....	20
2.4 Impedance spectroscopy and its application to organic solar cells .....	22
<b>3 Materials, device preparation and experimental methods.....</b>	<b>27</b>
3.1 Materials .....	27
3.1.1 Absorber layer: Polymer:fullerene blends .....	27
3.1.2 Hole and electron transport layers: polymer dispersions and solution-based TiO <sub>x</sub> .....	28
3.1.3 Contact materials .....	29
3.2 Device preparation.....	29
3.3 Experimental methods .....	32
<b>4 Results and discussion .....</b>	<b>34</b>
4.1 Equivalent circuit model for the quantification of the s-shape effect in TiO <sub>x</sub> containing inverted solar cells .....	34
4.2 The influence of the hole transport layer on solar cell performance and stability .....	44
4.3 The influence of the PSS content in PANI:PSS on the performance and stability of organic solar cells .....	60
<b>5 Conclusions.....</b>	<b>69</b>
<b>Bibliography.....</b>	<b>71</b>

<b>Publications and conference contributions.....</b>	<b>81</b>
<b>Acknowledgements.....</b>	<b>84</b>
<b>Curriculum vitae .....</b>	<b>86</b>
<b>Erklärung.....</b>	<b>88</b>

# 1 Introduction

Climate change, anthropogenic greenhouse gas emission and increasing energy demand are among the most pressing issues humanity is facing nowadays which have to be solved within the next decades<sup>[1]</sup>. Renewable energies are seen as one of the answers to these problems<sup>[2]</sup>. Among the various technologies in the field of renewable energy, photovoltaics, which embraces the direct conversion of sunlight into electricity, is very promising. However, over the short term, the generation of electricity through burning fossil fuels is still cheaper than the initial investment for the setup of solar power plants.

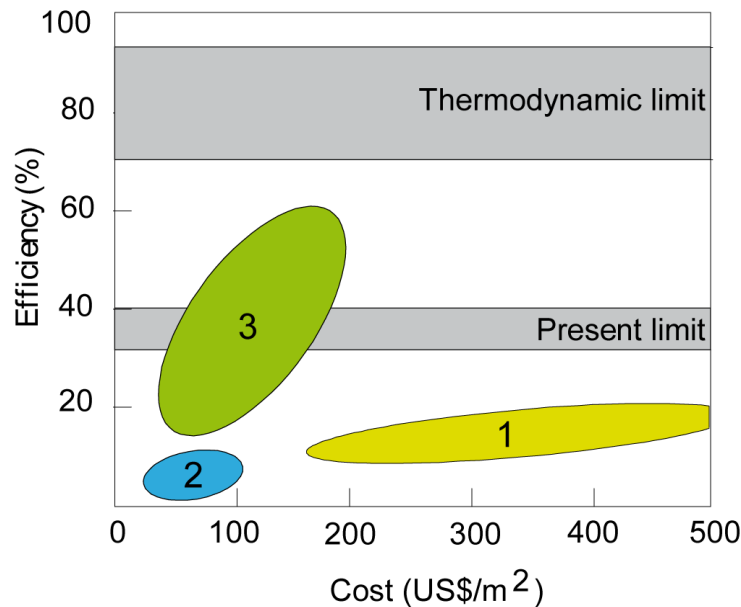


**Figure 1: Cost vs. efficiency for the different generations of photovoltaic technologies; 1: wafer based mono-crystalline silicon, 2: thin films, 3: emerging thin films<sup>[3]</sup>.**

Therefore further research on existing as well as the development of more sophisticated, so called third generation, solar cells is indispensable in order to make photovoltaics cost competitive with fossil fuels<sup>[3]</sup>. Next to solar cells based on inorganic semiconductors, like mono-crystalline silicon (first generation) or thin film technologies (second generation), among other third generation technologies

the use of organic semiconductors could expand the field of applications, as it offers properties such as light weight, flexibility, semi transparency and low production costs leading to short amortization times<sup>[4]-[6]</sup>. Figure 1 gives an overview of the different technology generations and their relation of efficiency vs. cost. Third generation technologies aim at high efficiency combined with lowering their cost due to decreased material consumption and improved photon harvesting capabilities. Recently, the power conversion efficiency of single and tandem organic solar cells reached certified values of 8.3% and 9.8%, respectively, and is just becoming competitive to enter the market, with first products already commercially available<sup>[7]-[9]</sup>.

In order to further increase the power conversion efficiency of organic solar cells, the synthesis of strong absorbers with low energy band gaps, harvesting more of the sun`s solar radiation spectrum is necessary and has become a major field of research within the community<sup>[10],[11]</sup>. As the power conversion efficiency of organic solar cells is ascending towards 10%, which is a market analyst`s benchmark predicting economic success of organic photovoltaics, more and more attention is drawn to lifetime and stability issues<sup>[6]</sup>. Although outdoor lifetimes of flexible organic solar cells exceeding one year were already presented, we are far away from understanding the underlying mechanisms leading to the degradation of organic solar cell performance<sup>[12]-[14]</sup>.

From an engineering point of view it is important to find materials which provide proper encapsulation while maintaining both the device flexibility and ease in implementation of the process in a roll-to-roll production line. Nonetheless it is highly important to investigate and understand the processes leading to the degradation of both the materials and the fully assembled organic solar cells, in which also interfaces become relevant<sup>[15]-[17]</sup>.

The thesis at hand aims to add insights for the improvement of the lifetime of organic solar cells as well as to uncover underlying degradation mechanisms. To do

so, the focus lies mainly on the investigation of the hole and electron selective transport layers sandwiching the photoactive layer, adopting novel materials and device architectures. Impedance spectroscopy is used as a non-destructive, powerful technique to study fully processed organic solar cells.

## 2 Fundamentals of organic photovoltaics and impedance spectroscopy

An almost unlimited amount of organic compounds are naturally existent or can be synthesized. They consist mainly of a carbon atom based backbone, of which they received their name according to the field of organic chemistry. A special group within organic solids are organic semiconductors<sup>[18]</sup>. This chapter offers a basic introduction to organic semiconductors as well as to their application in organic photovoltaics. Stability issues of organic solar cells and impedance spectroscopy applied on organic solar cells are discussed later on.

### 2.1 Organic semiconductors

The (photo-) conductivity in organic crystals has been studied for almost 100 years<sup>[19],[20]</sup>, however, these systems are usually used as model systems. The discovery of conducting polymers in the late 1960s by Weiss et al.<sup>[21]–[23]</sup> and further work in the 1970s by McGinnes et al.<sup>[24],[25]</sup> and Shirakawa, MacDiarmid and Heeger et al.<sup>[26],[27]</sup> paved the way to electronic devices using organic semiconductors. Tang et al.<sup>[28],[29]</sup> reported on organic light emitting diodes and organic photovoltaic cells in the 1980s. Since then the field emerged to a major division of solid state physics.

Organic semiconductors can be divided into two major classes, namely small molecules and macromolecules<sup>[18]</sup>. Macromolecules are usually thermally instable and are, contrary to small molecules, not suited for sublimation in high vacuum for the preparation of thin films. Hence, macromolecules, amongst others polymers, are synthesised with functional side groups enhancing their solubility, which allows wet-processing from solution via spin coating or roll-to-roll compatible blading or printing techniques<sup>[30]</sup>. This way of thin film processing however induces a certain degree of disorder in polymeric thin films, strongly influencing their physical properties, which will be discussed later on.

Figure 2 shows the formation of a double bond in the simplest possible molecule ethene, where each carbon atom encounters three  $\sigma$  bonds originating from the electrons within the degenerated  $sp^2$  orbitals creating the backbone of the organic molecule via strong covalent bonds. One  $\sigma$  bond connects to each of the hydrogen atoms and one  $\sigma$  bond is formed between the carbon atoms. The fourth valence electron of each carbon atom situated in the respective  $p_z$  orbital, which is oriented perpendicular to the  $sp^2$  orbitals, form a  $\pi$  bond, which is weaker than the  $\sigma$  bond due to lesser overlap of the  $p_z$  orbitals. Along with the formation of the  $\sigma$  and  $\pi$  bonds the respective orbitals split into bonding and antibonding (denoted with \*) orbitals, whereas the splitting of the  $\sigma$  and  $\sigma^*$  orbitals is stronger than the splitting of the  $\pi$  and  $\pi^*$  orbitals according to the bonding strength. Thus the  $\sigma$  orbital is located deeper in energy than the  $\pi$  orbital and the anti-bonding orbitals are located higher in energy as can be seen in the energy diagram on the right hand side of Figure 2. Thus the transition from the bonding  $\pi$  orbital to the anti-bonding  $\pi^*$  orbital constitutes the band gap, separating the highest occupied molecular orbitals (HOMO) and the lowest unoccupied molecular orbitals (LUMO) states.

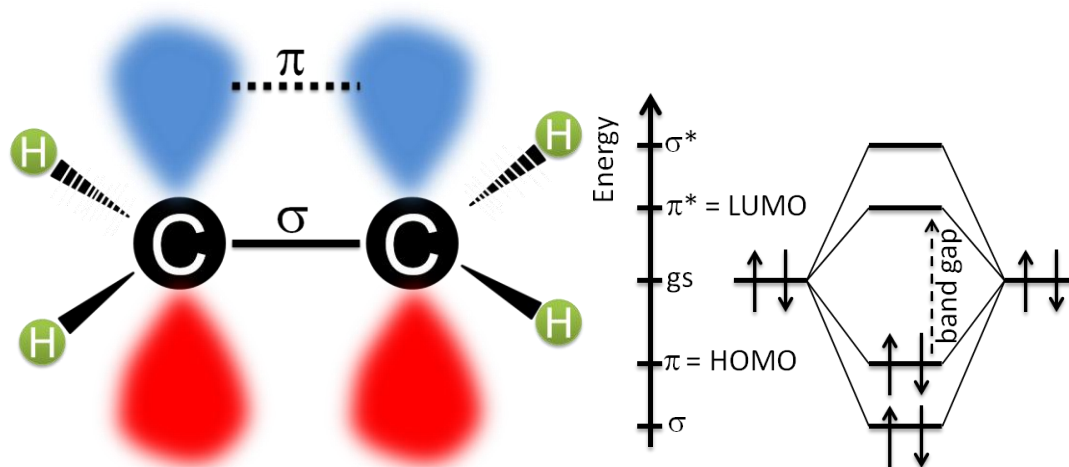


**Figure 2: Simplified schematic of the formation of a  $\sigma$  and a  $\pi$  bond in an ethene molecule (left), and an simplified energy diagram (neglecting the hydrogen bonds) showing HOMO and LUMO levels separated by a band gap, gs defines the ground state.**

The band gap energy of organic semiconductors lies in the range of 1 eV to 3 eV, which corresponds to the visible wavelength range, making them attractive for opto-electronic applications. Optical excitation with a photon having an energy above the band gap energy leads to the formation of a strongly bound (approx. 0.5eV to 1eV) electron hole pair, called Frenkel exciton. Due to the strong Coulombic interaction the Frenkel exciton only exhibits a radius of around one nanometer. This is in contrast to inorganic semiconductors, where the much larger dielectric constant screens the Coulombic interaction leading to the formation of Wannier excitons, distributed over several crystal sites, with energies well below thermal energy at room temperature ( $k_bT \sim 300\text{meV}$ ). Thus, the thermal energy suffices to dissociate the Wannier excitons into free charges.

In order to facilitate exciton dissociation in organic semiconductors, which is an elementary process in organic solar cells discussed later, a so called donor acceptor system is utilized. Bringing in contact two kinds of organic semiconductors with different HOMO and LUMO levels one can define this as donor acceptor system. An acceptor then exhibits a larger electron affinity than the donor, which in turn exhibits a weaker ionization energy than the acceptor. A Frenkel exciton, generated on a donor site can then be split via transfer of the electron from the donor's LUMO to a neighbouring acceptor's LUMO. The positive charge remains on the HOMO of the donor.

In the mid-1990s detailed studies on charge transfer showed that using a fullerene as acceptor leads to an ultrafast charge transfer from the donor to the fullerene. The electron is transferred in the femto-second range to the acceptor, whereas back transfer to the donor, which acts as a loss channel, occurs only in the order of microseconds, thus resulting in an almost 100% efficiency in exciton dissociation<sup>[31]</sup>.

In organic semiconductors exhibiting strong disorder as is the case for polymers, free charges, i.e. electrons and holes, are named negative and positive polaron, respectively. Polarons are quasi-particles which consist of the charge carrier combined with the lattice distortion induced in the medium by the charge.

In order to describe charge transport in organic semiconductors it becomes first necessary to look at the molecular structure of organic semiconductors. Common to organic semiconductors is an alternation of single and double bonds, which leads to the formation of a conjugated  $\pi$  electron system. Within the conjugated system the  $\pi$  bonds are delocalized throughout the whole molecule. Promoting negative charges from the HOMO into the LUMO via charge injection, doping or formation and splitting of excitons, allows them to move within the delocalized  $\pi^*$  orbital representing the LUMO level. However, due to the energetic and structural disorder in polymeric thin films with broad distributions in molecular weight, orientation and polarizability, single polymer chains exhibit for example twists or kinks, which disrupt the conjugated system and thus the delocalization.

Charge transport is therefore described by hopping transport meaning the phonon-assisted tunnelling of charges between localized energy sites. The hopping rate of carriers in a disordered medium is often described by the Miller-Abraham formalism<sup>[32],[33]</sup>:

$$\nu_{ij} = \nu_0 \cdot \exp\left(-2 \cdot \gamma \cdot a \cdot \frac{r_{ij}}{a}\right) \cdot \begin{cases} \exp\left(\frac{-E_{ij}}{k_B \cdot T}\right) & , E_{ij} > 0 \\ 1 & , E_{ij} < 0 \end{cases} \quad (1)$$

, where  $\nu_{ij}$  is the hopping rate between occupied site  $i$  and unoccupied site  $j$ ,  $\nu_0$  is the attempt-to-hop frequency,  $\gamma$  is the inverse localisation radius of the charge carrier in the respective energy site,  $a$  is the average lattice constant,  $r_{ij}/a$  is the distance between site  $i$  and site  $j$  and  $E_{ij}$  is the energetic difference of site  $i$  and site  $j$ <sup>[32],[34]</sup>. Monroe demonstrated that the hopping rate is maximized with respect to a single energy, called transport energy  $E_T$ <sup>[35]</sup>. This is mathematically equal to band

transport with multiple trapping and release. In disordered organic materials the density of states is assumed to be Gaussian due to the shape of the absorption bands. Baranovskii et al. later showed that the concept of transport energy can be extended to density of states with a Gaussian distribution allowing to describe charge transport in organic semiconductors with multiple trapping and release processes<sup>[34],[36]</sup>.

A charge carrier placed at a higher energy would relax to a certain relaxation energy, and transport occurs at energies close to the transport energy, at energies below the maximum of the Gaussian density of states, as shown in Figure 3<sup>[35],[37]</sup>–<sup>[39]</sup>.

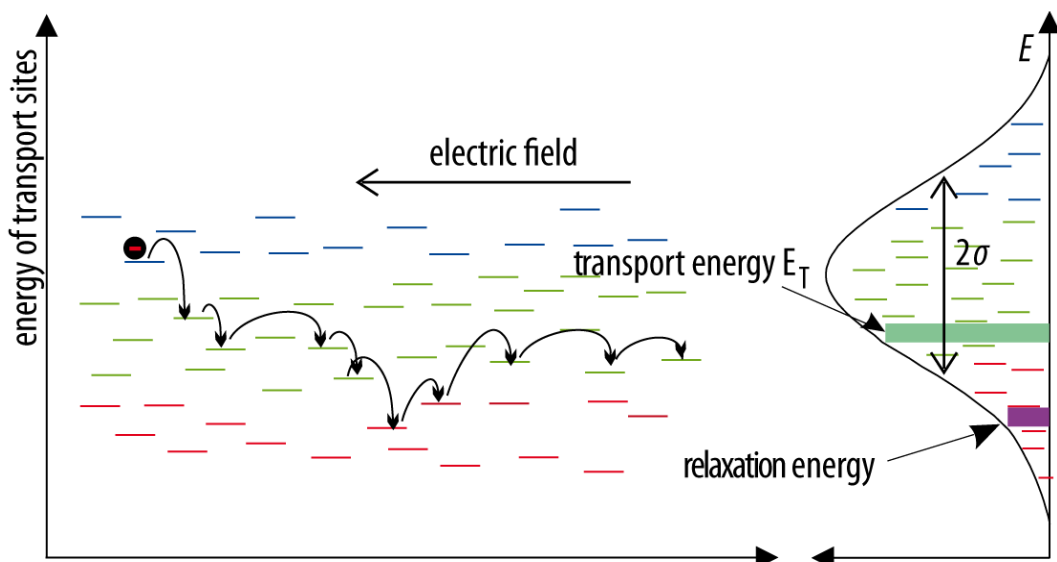


Figure 3: Schematic of charge transport between energetic and structural disordered states (left). Representation as Gaussian density of states (DOS) denoted as  $g(E)$  showing the transport energy level  $E_T$  just below the maximum of the distribution<sup>[38]</sup>.

## 2.2 Organic photovoltaics

In this chapter the elementary processes in organic solar cells are presented followed by the presentation of the bulk-heterojunction device concept.

### 2.2.1 Elementary processes in organic solar cells

Figure 4 presents a schematic energy diagram of the elementary processes from light absorption to charge extraction of a donor acceptor system used in organic photovoltaics<sup>[40]</sup>. The absorption of an incoming photon with energy large enough to excite an electron from the donor's HOMO to the donor's LUMO leads to the formation of a Frenkel exciton. The neutral exciton has to diffuse to a donor acceptor interface within its lifetime, usually corresponding to a diffusion length in the range of a few tens of nanometers<sup>[41]-[43]</sup>.

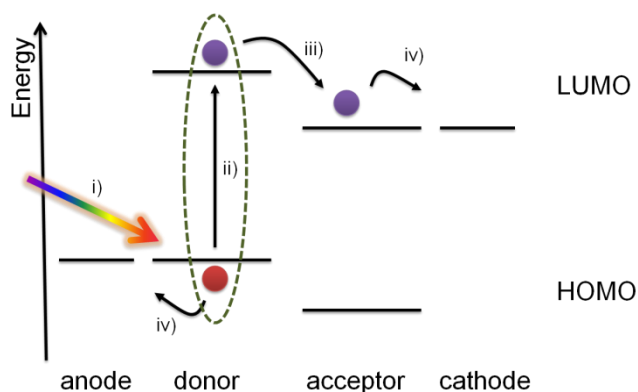


**Figure 4: Simplified energy diagram showing the four elementary processes in a organic solar cell: i) light absorption, ii) exciton formation, iii) exciton dissociation at a donor acceptor interface and iv) charge extraction.**

The donor acceptor interface has to provide enough energy to overcome the Coulombic binding energy for the dissociation of Frenkel excitons, due to the offset of the LUMO levels of the donor and acceptor. Once the exciton is dissociated positive and negative polarons are formed in the donor and acceptor phase, respectively, which still are Coulombically bound polaron pairs<sup>[44]</sup>.

Due to the internal electric field set up by the work function difference of the electrodes, the polaron pairs are dissociated and positive polarons drift to the anode

and negative polarons drift to the cathode, respectively. Finally, the polarons have to be extracted from the bulk-heterojunction. For efficient extraction ohmic contacts between the electrodes and the active layer are necessary, thus the anode has to match the HOMO level of the donor and the cathode has to match the LUMO level of the acceptor, respectively, as shown in Figure 4<sup>[4].[45]</sup>.

### 2.2.2 The bulk-heterojunction concept

The low diffusion length of excitons in solution processed, disordered materials, such as polymers, demands a device structure in which exciton dissociation is still efficient. In order to enable the dissociation of ideally all generated excitons throughout the active layer, blending of the donor and acceptor materials was introduced in the mid 1990ies<sup>[46]</sup>. This led to the formation of the bulk-heterojunction, where donor and acceptor phases were dispersed within the whole active layer and a three dimensional network of interfaces is created as depicted in Figure 5. Ideally all photo-generated excitons can diffuse to a donor acceptor interface within their lifetime for efficient dissociation, allowing at the same time thicker active films for higher photon absorption.

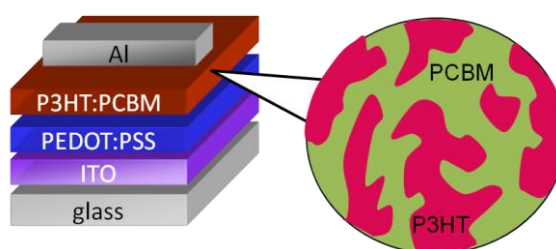


**Figure 5: A solar cell stack with a bulk-heterojunction as active layer showing dispersed donor and acceptor regions in the detail.**

A broad field of research in organic photovoltaics is concerned with morphology investigations and control<sup>[47]</sup>. Donor and acceptor domains should, on the one hand, be dispersed finely enough to maximize the interface for efficient exciton dissociation, and on the other hand, percolation pathways should be present so

that the dissociated charges can be transported within the donor or acceptor phase to the respective electrodes. If the morphology is not optimized, recombination of charge carriers can reduce the power conversion efficiency<sup>[48]</sup>.

Increases in the power conversion efficiency of bulk-heterojunction solar cells have resulted from techniques to improve the photocurrent. One strategy is the use of novel compounds with an increased light harvesting capability. Other strategies have focussed on creating well-ordered bulk-heterojunctions via self-assembly, soft-lithography or nano-imprinting techniques<sup>[49]–[52]</sup>.

Additionally, next to the control of the morphology of the active layer, interlayers connecting the active layer and the electrodes with charge selective or charge blocking properties have been studied intensively<sup>[53],[54]</sup>. With the beginning of the century the introduction of a LiF interfacial layer with a thickness below one nanometer between the active layer and the aluminium cathode was shown to increase solar cell performance, although, it is still somewhat unclear how the LiF interacts in the device<sup>[55]</sup>. For improving the hole extraction capabilities a 30 nm

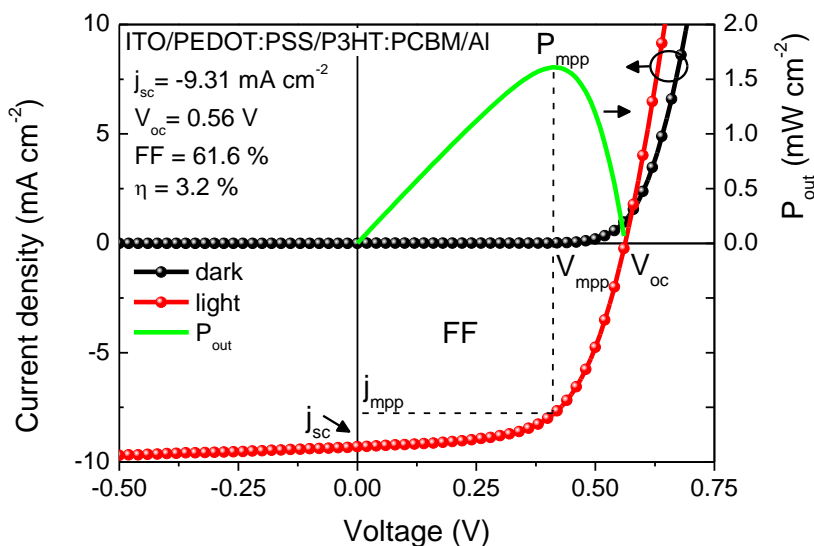


**Figure 6: IV-characteristics of an organic bulk-heterojunction solar cell in dark and under illumination, additionally the output power and solar cell parameters are shown.**

to 50 nm thin PEDOT:PSS hole transport layer was introduced connecting the ITO anode and the active layer. This became a standard interlayer since the early days of organic solar cells. However, as was shown in literature and will be shown in this thesis, the PEDOT:PSS layer can strongly impact the stability of the solar cell<sup>[56]</sup>.

Figure 6 presents an exemplary IV characteristics of a bulk-heterojunction solar cell prepared as described in chapter 3.2 under dark and illuminated conditions<sup>[40],[57]</sup>. From the illuminated IV curve the solar cell parameters can be extracted. The intersection of the curve with the voltage-axis gives the open circuit voltage ( $V_{oc}$ ). The intersection with the current density-axis gives the short circuit current density ( $j_{sc}$ ). The fill factor (FF) is defined as the ratio of the voltage ( $V_{mpp}$ ) times current density ( $j_{mpp}$ ) giving the maximum power point ( $P_{mpp} = V_{mpp} \cdot j_{mpp}$ ) and the open circuit voltage ( $V_{oc}$ ) times the short circuit current density ( $j_{sc}$ ) of the solar cell.

$$FF = \frac{V_{mpp} \cdot j_{mpp}}{V_{oc} \cdot j_{sc}} \quad (2)$$

The power conversion efficiency ( $\eta$ ) is defined as the ratio of the generated power  $P_{out}$  to the incoming power  $P_{in}$  striking the solar cell.

$$\eta = \frac{V_{oc} \cdot j_{sc} \cdot FF}{P_{in}} = \frac{V_{mpp} \cdot j_{mpp}}{P_{in}} = \frac{P_{out}}{P_{in}} \quad (3)$$

### 2.3 Degradation mechanisms in organic solar cells

With the tremendous effort over the last few years in achieving higher power conversion efficiencies in organic solar cells, studies on device lifetime and degradation mechanisms shifted more into focus. Only the understanding of these degradation mechanisms can ensure that the stability and lifetime of organic solar cells can be increased to several years<sup>[14]</sup>.

Recently, the number of publications dealing with degradation mechanisms or stability issues of organic solar cells has been rising. From a technical point of view degradation of organic solar cells can be greatly avoided using encapsulating barrier foils with low permeation rates for oxygen and humidity<sup>[58],[59]</sup>. On the one hand, these high performance barriers are often more expensive than the organic solar cells itself and on the other hand often restrict the flexibility of the encapsulated solar cells and modules. In order to introduce cheaper, less efficient, encapsulation foils, one has to find the tolerance levels of oxygen and humidity of the sensitive materials used and to investigate the mutual effects in complete devices.

Up to now investigations often concerned the influence of extrinsic parameters like temperature, light, oxygen and humidity on single active layers, on interfaces and contacts, or on fully processed solar cells<sup>[15],[17],[60]–[63]</sup>. Figure 7 presents several degradation mechanisms which were isolated in literature<sup>[14]</sup>. However, fewer publications deal with intrinsic degradation mechanisms arising from the materials used to produce solar cells. Additionally the interfaces between materials can also be a bottle neck for improving device lifetime, but it is generally difficult to localize and characterize stability issues in complete devices.

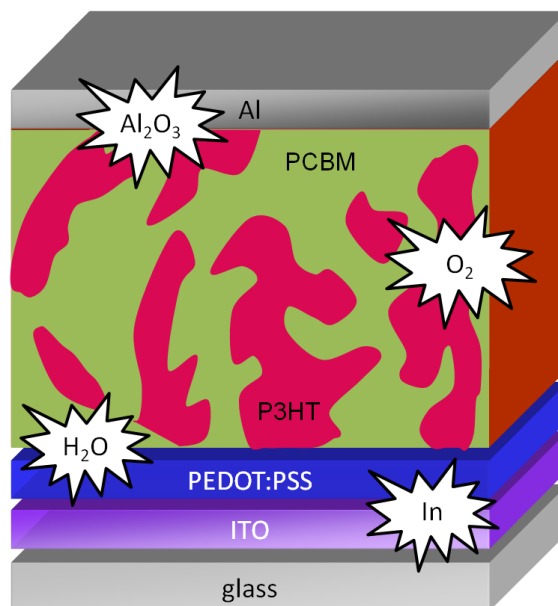


**Figure 7: Schematic of an organic solar cell stack showing different degradation mechanisms.**

## 2.4 Impedance spectroscopy and its application to organic solar cells

Many experimental techniques have been used to study degradation mechanisms in organic thin films and in organic solar cells. Impedance spectroscopy has been receiving increasing attention for studying organic solar cells and is also applied in this thesis. Here, a basic introduction to impedance spectroscopy is given.

Impedance is defined as the ratio of voltage and current, according to Ohm's law and is usually a complex magnitude (except for ideal resistors) and macroscopically describes the behavior of charge carrier transport in dielectrics and (semi-)conducting materials.

$$Z = \frac{V}{I} = \text{Re}\{Z\} + i \cdot \text{Im}\{Z\} \quad (4)$$

, where  $V$  over  $I$  is the voltage and current, respectively,  $\text{Re}\{Z\}$  is the real part and  $\text{Im}\{Z\}$  is the imaginary part of the impedance, both in units of  $[\Omega]$  and  $i$  is the

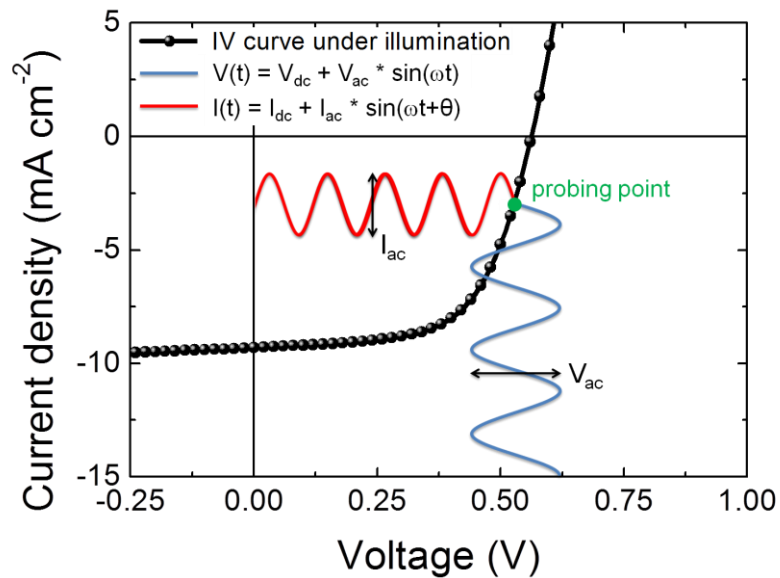


**Figure 8:** Schematic of an impedance spectroscopy measurement. The applied ac voltage at a certain probing point on the IV curve of the device under test results in an ac current, which combines with the applied ac voltage to the complex resistance<sup>[64]</sup>.

complex number<sup>[64]</sup>.

A small signal sinusoidal AC voltage with amplitude  $V_{ac}$ , (which can be superimposed by a DC component  $V_{dc}$ ) is applied to the sample:

$$V(t) = V_{dc} + V_{ac} \cdot \sin(\omega t) \quad (5)$$

The resulting current  $I(t)$  consists of a certain DC offset current  $I_{dc}$  and an AC current with amplitude  $I_{ac}$ , which is shifted by an phase angle  $\theta$  with respect to  $V(t)$ :

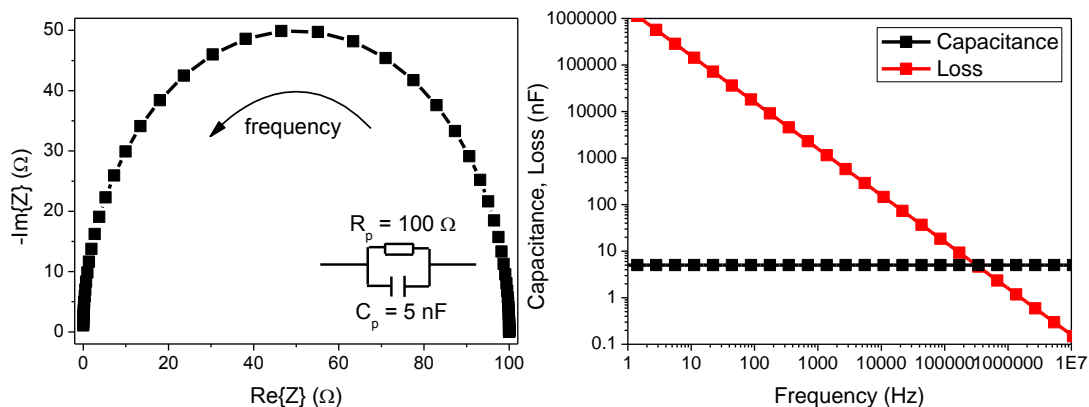
$$I(t) = I_{dc} + I_{ac} \cdot \sin(\omega t + \theta) \quad (6)$$

Figure 8 illustrates this principle. Using a DC offset allows one to probe regions of interest along the IV-curve of a solar cell, e.g. under short circuit or open circuit conditions.

There are several parameters related to impedance ( $Z=R-i\cdot X$ , where  $R$  is the resistance and  $X$  is the reactance), such as admittance ( $Y=Z^{-1}=G+i\cdot B$ , where  $G$  is the conductivity and  $B$  is the susceptance), modulus ( $M=i\cdot\omega\cdot C\cdot Z$ , with  $\omega=2\cdot\pi\cdot f$  as the angular frequency and  $C$  as capacitance) and complex dielectric permittivity ( $\epsilon=M^{-1}=Y/(i\cdot\omega\cdot C)$ ), all together known as immittance. In this thesis, mainly the impedance and the capacitance  $C=1/(i\cdot\omega\cdot X)$  as well as the dielectric loss ( $L=1/(\omega\cdot R)=\tan(\delta)\cdot C$ , with  $\tan(\delta)=\text{Re}\{Z\}/\text{Im}\{Z\}$  as the loss tangent) are investigated. The frequency dependence of these parameters is particularly useful in analyzing transport and degradation processes related to layers and interfaces in the solar cell. Capacitance reveals information about stored or trapped charge in the device while loss reveals information on energy loss due to transport limited phenomena. In this thesis, focus will therefore be placed on the capacitance and loss<sup>[64]</sup>.

Equivalent circuit modeling is often used in conjunction with impedance spectroscopy to quantitatively describe the impedance data. To demonstrate this, a simple

equivalent circuit consisting of a resistor and capacitor in parallel, often used to describe organic layers, is depicted in Figure 9 together with the corresponding representations in the complex plane, i.e. the Cole-Cole plot, and the capacitance and loss plotted versus frequency in a Bode plot.



**Figure 9:** Typical representations as Cole-Cole plot in the complex plane (left) and Bode plots of capacitance and loss (right). The inset shows the equivalent circuit  $R_p$ - $C_p$  with  $R_p = 100 \Omega$  and  $C_p = 5 \text{ nF}$ .

The  $R_p$ - $C_p$  element results in a single semicircle in the complex plane. At low frequencies, the crossing of the semicircle with the real axis gives the value for the resistance  $R_p$  (here  $R_p=100\Omega$ ), the center of the semicircle corresponds to the time constant  $\tau = R_p \cdot C_p$ . At higher frequencies the capacitance  $C_p$  dominates. Similar results can be obtained from the frequency-dependent representation of the capacitance and the loss. To model real devices, usually more than one  $R_p$ - $C_p$  element has to be added to an equivalent circuit model to account for multiple layers and interfaces in order to mimic the complete behavior of the sample.

Cole and Cole developed an equivalent circuit which enables to account for dispersive transport in disordered organic semiconductor films, which is shown in Figure 10<sup>[65]</sup>. It consists of an  $R_b$ - $C_{\text{geo}}$  element in parallel to a capacitance  $C_{\text{dis}}$  in conjunction with a constant phase element  $\text{CPE}_{\text{dis}}$ .

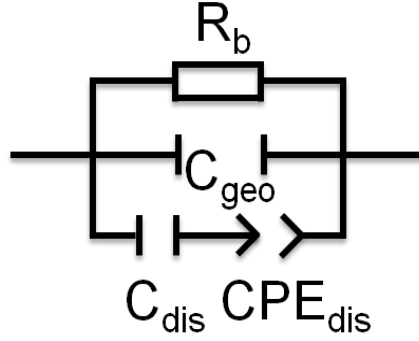


**Figure 10: Equivalent circuit model accounting for dispersive transport<sup>[65]</sup>.**

$R_b$  describes the resistance of the organic thin film,  $C_{geo}$  is the geometrical capacitance, according to  $C_{geo} = (\epsilon_0 \cdot \epsilon_r \cdot A)/d$  with  $\epsilon_0$  as dielectric permittivity,  $\epsilon_r$  as the dielectric constant of the organic material,  $A$  as the active area and  $d$  as the thickness of the organic layer. The  $CPE_{dis}$  is used to describe a non-ideal capacitor with a capacitive contribution  $CPE-T_{dis}$  and the quality factor  $CPE-P_{dis}$ , which can adopt values between zero and one. The compound circuit element accounts for dispersive transport in organic media and is part of the equivalent circuit model proposed in chapter 4.1<sup>[64]–[66]</sup>. Chen et al.<sup>[67]</sup> recently used this compound circuit element in order to describe dispersive transport in doped organic films. Martens et al.<sup>[68]</sup> and Berleb and Brütting<sup>[69]</sup> applied equation (7), which is the mathematical analogue to the equivalent circuit shown in Figure 10, to describe dispersive transport in poly(p-phenylene vinylene) (PPV) and tris(8-Hydroxyquinoline) Aluminum ( $Alq_3$ ):

$$\epsilon - \epsilon_{\infty} = \frac{\epsilon_s - \epsilon_{\infty}}{1 + (i \cdot \omega \cdot \tau_0)^{1-\alpha}} \quad (7)$$

, where  $\epsilon$  is the dielectric constant,  $\epsilon_{\infty}$  is the high frequency dielectric constant,  $\epsilon_s$  is the low frequency dielectric constant,  $i$  is the imaginary number,  $\omega$  is the angular frequency,  $\tau_0$  is the average relaxation time and the parameter  $\alpha$  can adopt values between 0 and 1 accounting for the distribution of relaxation times around  $\tau_0$ .

The right side of equation (7) describes the dispersive nature of the organic media in the transition from the low frequency static regime described by  $\epsilon_s$  to the high frequency limit  $\epsilon_\infty$ , according to the geometrical capacitance  $C_{\text{geo}}$ .

The investigation and comparison of intrinsic and extrinsic degradation mechanisms in organic solar cells using impedance spectroscopy is the main topic of this thesis, focussing on the influence of the electron and hole extraction layers.

Chapter 4.1 presents a model system with a  $\text{TiO}_x$  interlayer applied as electron selective extraction layer in an inverted solar cell structure. The properties of the  $\text{TiO}_x$  interlayer result in IV characteristics which initially show an s-shape effect. The s-shape disappears upon light soaking with UV light. The effect is reversible if the devices are stored in the dark for a period of time. An equivalent circuit model is proposed to explain the s-shape effect in this model system, which usually can appear upon degradation of solar cells.

In the following sections several hole transport layers and their influence on solar cell parameters are discussed. The influence of the solvent from which the hole transport layer is prepared (section 4.2) and the ratio of poly(styrenesulfonate) (PSS) to polyaniline (PANI) (section 4.3) on the performance and stability of solar cells is shown.

### 3 Materials, device preparation and experimental methods

This chapter presents the used materials and describes the solar cell preparation, followed by the description of the applied measurement techniques.

#### 3.1 Materials

The materials applied in this study are either already commercially available, developed within a cooperation or are, as in the case of  $\text{TiO}_x$ , synthesized from commercially available precursors.

##### 3.1.1 Absorber layer: Polymer:fullerene blends

Figure 11 shows the chemical structures of the active layer materials. For the investigations regio-regular poly(3-hexylthiophen) (P3HT) blended with a soluble fullerene derivative [6,6]-phenyl-C61-butyric acid methyl ester (PCBM) was dissolved in anhydrous chlorobenzene (CB) or 1,2-dichlorobenzene (oDCB). P3HT used for the study presented in chapter 4.1 was provided by Merck Chemicals Inc. (Lisicon SP001, regio-regularity=94.2%,  $M_n=23600$ ,  $M_w=54200$ , polydispersity=2.29), P3HT used for the investigations discussed in the chapters 4.2 and 4.3 was purchased as electronic grade, regio-regular P3HT from Rieke Metals Inc. (4002-E, regio-regularity=90-94%,  $M_w=50000$ ). PCBM was purchased from Solenne B.V. ( $M_w=910.9$ ), CB as well as oDCB from Sigma-Aldrich.

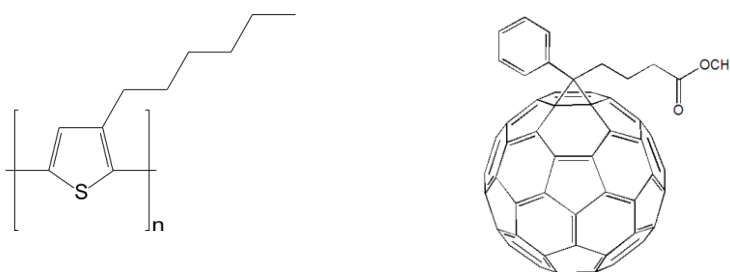


**Figure 11: Chemical structures of P3HT and PCBM used for the active layer.**

### 3.1.2 Hole and electron transport layers: polymer dispersions and solution-based TiO<sub>x</sub>

The hole transport layers investigated in chapter 4.2 and 4.3 were either commercially available Poly(3,4-ethylenedioxythiophene):poly(styrenesulfonate) PEDOT:PSS purchased as Clevios P VP AI 4083 through H.C. Stark or various poly(aniline): poly(styrenesulfonate) PANI:PSS formulations obtained from Enthone Nano Science Center, Ammersbek, a subsidiary of Cookson Electronics. The chemical structures are shown in Figure 12 and several properties are summarized in Table 1 and Table 2.

**Table 1: Properties of the hole transport layers used in chapter 4.2. [a] layer thickness: 100nm; measured from 400nm - 900 nm, [b] measured by Kelvin probe in air at 0% relative humidity and room temperature, [c] measured in vacuum at room temperature.**

The sol-gel synthesis of titanium-sub-oxide (TiO<sub>x</sub>) used as electron extraction layer was carried out with materials purchased from Sigma-Aldrich Inc. without further purification: titanium (IV) isopropoxide (Ti[OCH(CH<sub>3</sub>)<sub>2</sub>]<sub>4</sub>), 2-methoxyethanol (CH<sub>3</sub>OCH<sub>2</sub>CH<sub>2</sub>OH) and ethanolamine (H<sub>2</sub>NCH<sub>2</sub>CH<sub>2</sub>OH). The TiO<sub>x</sub> precursor was prepared following the route of Park et al.<sup>[70]</sup> and diluted in methanol prior spin coating.

hole transport layer	Solvent	pH value	Transmittance [%] [a]	Solid content [wt%]	Work function [eV] [b]	Conductivity [S/cm] [c]
PEDOT:PSS (H <sub>2</sub> O)	water	1.5	94	1.5	4.81	3.9 E-4
PANI:PSS (H <sub>2</sub> O)	water	1.6	76	3.0	5.08	3.0 E-2
PANI:PSS (IPA)	2-propanol	-	86	2.3	5.49	1.6 E-3

**Table 2: Properties of the hole transport layers used in chapter 4.3. [a] layer thickness: 100nm; measured from 400nm - 900 nm, [b] measured by Kelvin probe in air at 0% relative humidity and room temperature, [c] measured in vacuum at room temperature.**

hole transport layer	Solvent	PANI:PSS ratio	Transmittance [%] <sup>[a]</sup>	Work function [eV] <sup>[b]</sup>	Conductivity [S/cm] <sup>[c]</sup>
PANI:PSS 1:1	water	1:1.4	90	5.080	4.0 E-02
PANI:PSS 1:2	water	1:2.2	91	5.190	2.0 E-04
PANI:PSS 1:5	water	1:5.1	95	5.060	2.0 E-05

### 3.1.3 Contact materials

For the contacts, indium tin oxide (ITO) coated glass substrates were obtained from Präzisions Glas & Optik GmbH, and calcium (Ca), aluminum (Al), silver (Ag) and molybdenum oxide ( $\text{MoO}_3$ ) were thermally deposited to create back contacts.

### 3.2 Device preparation

For the investigations carried out in chapter 4.2 and 4.3 solar cells in the standard geometry as shown in Figure 13a) were prepared. The solar cells used in chapter 4.1 were prepared in the inverted structure as shown in Figure 13b). In the following the different preparation routes are described and Figure 14 presents IV characteristics of exemplary solar cells in the standard and inverted geometry.

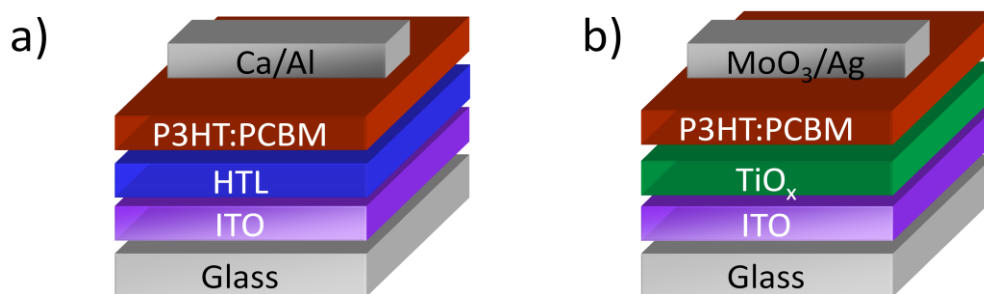


**Figure 12: Schematic of the a) standard and b) inverted solar cell stacks (HTL: hole transport layer).**

Prior solar cell preparation a 1 wt% solution with a P3HT:PCBM ratio of 2:1 for standard and a 1:1 ratio for inverted cells, respectively, was prepared under inert atmosphere in chlorobenzene and dichlorobenzene, respectively, and kept stirring overnight prior solar cell preparation.

ITO covered glass substrates were structured by etching in hydrochloric acid and mechanically cleaned with detergent and deionized water. Subsequent cleaning was done for 10 min in acetone and isopropyl alcohol using an ultrasonic bath followed by an oxygen plasma treatment for 15 min. For standard stacked solar cells hole transport layers (HTLs) were spin coated onto the cleaned substrates in ambient conditions at 3500 rpm for 30 s. As hole transport layers were used either PEDOT:PSS (applied using a 45  $\mu\text{m}$  pore filter) or hole transport layers based on PANI:PSS (without filtering), as shown in Table 1 and Table 2.

After deposition of the hole transport layer, the samples were brought into a nitrogen filled glove box, where all subsequent steps were carried out. The substrates covered with the hole transport layer were dried on a hot plate at 130° C for 10 min. The P3HT:PCBM solution was spin coated on top of the hole transport layers resulting in an active layer thickness around 100 nm, measured using a profilometer. The substrates were then transferred into an evaporation chamber.

Calcium and aluminum were evaporated on top of the active layer in vacuum at a pressure below  $10^{-6}$  mbar, with a thickness of 20 nm and 150 nm, respectively. The overlap of ITO and the metal cathode defined the solar cell active area to  $A = 0.5 \text{ cm}^2$ . The devices were then annealed on a hot plate at  $140^\circ \text{C}$  for 10 min.

For the preparation of inverted solar cells the  $\text{TiO}_x$  precursor was spin coated onto the etched and cleaned ITO substrates at 5000 rpm for 40 seconds. To convert the precursor into  $\text{TiO}_x$  via hydrolysis the substrates were then placed in a chamber set to a relative humidity of 45 % at a temperature of  $25^\circ \text{C}$  for a total of 2 hours. Then the substrates were transferred into a nitrogen filled glove box, where the following steps were carried out. The substrates were tempered at  $150^\circ \text{C}$  for 30 minutes in order to remove residual solvents from the precursor. The P3HT:PCBM blend was applied on top of the  $\text{TiO}_x$  via spin coating to create the active layer. The blend was then annealed at  $140^\circ \text{C}$  for 10 minutes prior mounting in an evaporation system connected to the glove box in order to evaporate the back contact consisting of 15 nm  $\text{MoO}_3$  and 150 nm Ag.

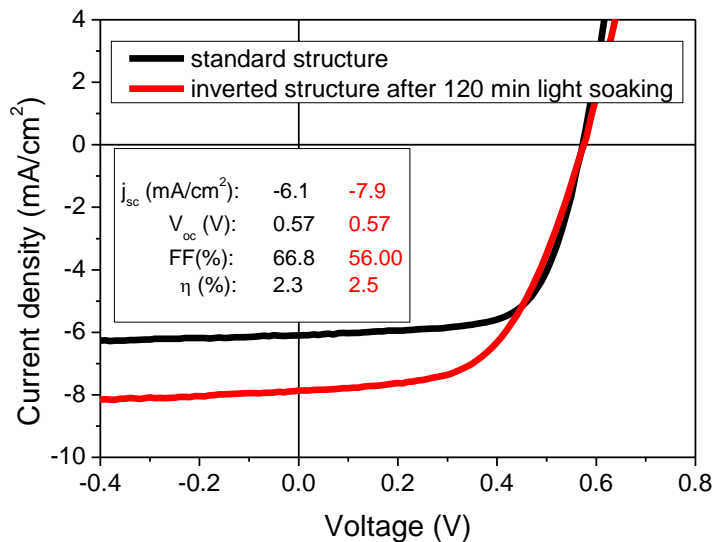


**Figure 13: IV characteristics of a standard and inverted solar cell prepared according to the description in chapter 3.2. The inset shows the extracted solar cell parameters.**

Encapsulation of the devices was also done under inert atmosphere using a 1:1 mixture of an epoxy resin and adequate hardener, which was sandwiched between the organic solar cell device and a cover glass plate, hardening at room temperature in dark overnight.

### **3.3 Experimental methods**

For illuminating the solar cells with simulated sun light a class AAA solar simulator (SS80 Photon Emission Tech. Inc.), emitting an AM1.5G spectrum, is used. The incoming power  $P_{in}$  is set to  $100 \text{ mW cm}^{-2}$  according to standard test conditions and is adjusted using a calibrated silicon solar cell traceable to Fraunhofer Institute of Solar Energy Systems, Germany. The sample temperature was monitored and kept at  $30^{\circ}\text{C} \pm 5^{\circ}\text{C}$  using air cooling. Electrical characterization of the solar cells was carried out using a Keithley semiconductor characterization system (SCS 4200) and a four probe contact configuration.

For impedance spectroscopy measurements a frequency response analyzer (Solartron 1260, Solartron Analytical) is used to measure in the frequency range from 30 MHz down to 1 Hz. Typically an AC voltage amplitude of  $V_{ac} = 100 \text{ mV}$  (RMS) or smaller was used to probe the solar cells. Again, a four probe configuration was used, in order to reduce cable effects.

For X-ray diffraction measurements a Panalytical X'Pert Pro was used in theta-2theta configuration. Atomic force micrographs were recorded using an Agilent Technologies 5420 AFM atomic force microscope in tapping mode. The film thickness was measured using a Dektak 6M stylus profiler.

For equivalent circuit analysis the software package ZView 3.1 of Scribner Associates is used, which allows one to combine different equivalent circuit elements, like resistors, capacitors or constant phase elements to compile an equivalent circuit and fit to experimental data.

For simulation of capacitance-voltage curves AFORSHET V2.2 provided as free download of the Helmholtz Zentrum Berlin is used.

## 4 Results and discussion

### 4.1 Equivalent circuit model for the quantification of the s-shape effect in $\text{TiO}_x$ containing inverted solar cells<sup>1</sup>

In this chapter, the formation of s-shaped current-voltage (IV) characteristics is investigated. In s-shaped IV curves a deflection point appears within the IV characteristic in the fourth quadrant resulting in a dramatic reduction of the fill factor and power conversion efficiency of the solar cell. In literature many reports on s-shaped IV characteristics in solar cells are present. This effect can appear upon exposure of solar cells to oxygen or water vapor, leading to the breakdown of the IV characteristics<sup>[13]</sup>. However, the origin of the s-shape effect is still under discussion.

Eisgruber et al.<sup>[71]</sup> presented an early study on the appearance of an s-shaped IV characteristic in inorganic CdS/CuInSe<sub>2</sub> thin film solar cells, occurring if the cell is exposed to red light and transformation to a regular shaped IV curve occurs after illumination with blue light. They concluded, that deep trap states in conjunction with low free electron concentrations in the CdS layer are responsible for the s-shape and blue light illumination significantly increases the electron concentration and thus the effect disappears. Glatthaar et al.<sup>[72]</sup> demonstrated, that impedance spectroscopy can be applied to investigate organic solar cells exhibiting an s-shaped IV characteristic and proposed that the reduced extraction of charge carriers leads to the s-shape.

---

<sup>1</sup>Reproduced in parts with permission from B. Ecker et al., Understanding S-Shaped Current–Voltage Characteristics in Organic Solar Cells Containing a  $\text{TiO}_x$  Interlayer with Impedance Spectroscopy and Equivalent Circuit Analysis, DOI:10.1021/jp305206d in J. Phys. Chem. C. Copyright 2012 American Chemical Society.

Further publications investigated the dependence of the s-shape effect on space charge limited currents, exciton blocking layer thickness, transport layer doping or imbalanced charge carrier mobility<sup>[73]–[76]</sup>. Steim et al.<sup>[77]</sup> recently demonstrated the presence of s-shaped IV characteristics in inverted organic solar cells containing a TiO<sub>x</sub> interlayer between the cathode and the active blend. Initial IV characteristics demonstrated an s-shape which disappeared upon light soaking under UV radiation. Based on the model system presented by Steim et al.<sup>[77]</sup> a detailed investigation using impedance spectroscopy and equivalent circuit analysis to describe how the TiO<sub>x</sub> interlayer influences the s-shape.

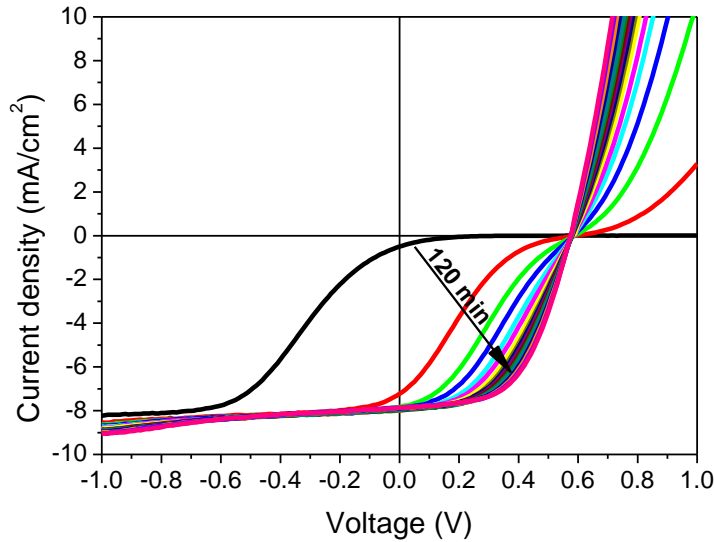


**Figure 14:** IV-characteristics of an inverted solar cell with a TiO<sub>x</sub> interlayer with improved solar cell parameters upon light soaking for 120 minutes.

In order to be able to investigate the s-shape effect in a controlled way, inverted solar cells with the device structure ITO/TiO<sub>x</sub>/P3HT:PCBM/MoO<sub>3</sub>/Ag as shown in Figure 13 b) are studied. The devices were prepared and encapsulated in a glove box as described in chapter 3.2, in order to ensure that only intrinsic properties of the solar cells are probed. The solar cells initially exhibit s-shaped IV characteristics, which then transform into regular IV characteristics upon UV irradiation.

tion due to a decrease in resistance of the  $\text{TiO}_x$  interlayer upon light soaking (Figure 15).

The  $\text{TiO}_x$ -based device works as a model system, in which effects leading to poor charge extraction, space charge build up, and s-shaped IV characteristics can be induced and controlled reproducibly. As already mentioned above, s-shaped IV characteristics usually appear upon degradation of solar cells in ambient conditions and lead to crucial reduction of the fill factor and hence the power conversion efficiency. Thus the model system, which is investigated here, allows quantitative access on how the  $\text{TiO}_x$  interlayer affects the IV characteristics under controlled conditions, as the formation of s-shaped IV characteristics upon degradation is still under debate. An equivalent circuit model is proposed to analyze the impedance data taken from devices before and after light soaking. It is demonstrated that it is possible to attribute its elements to specific sites in the solar cell, and therefore the circuit model can be used as a tool to localize and quantify loss mechanisms related to the  $\text{TiO}_x$  interface and s-shaped IV characteristics.

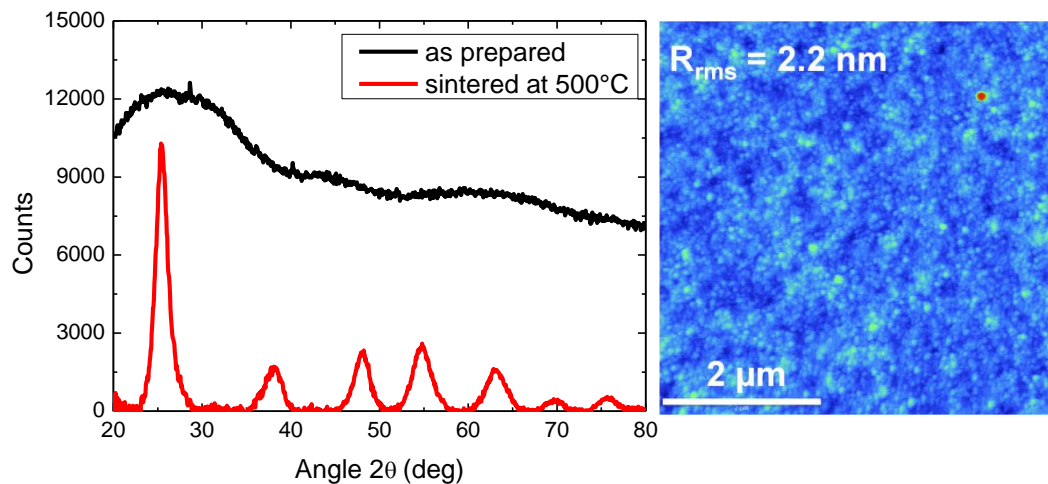


**Figure 15: XRD spectrum of amorphous  $\text{TiO}_x$  and sintered  $\text{TiO}_2$  after sintering the  $\text{TiO}_x$  at  $500^\circ \text{C}$  under ambient conditions (left), and topography of a  $\text{TiO}_x$  surface characterized with atomic force microscopy.**

In order to verify the synthesis of  $\text{TiO}_x$  from the sol-gel process described in chapter 3.1.2 first the structural and morphological properties of single  $\text{TiO}_x$  films being later applied as electron extraction layer in organic solar cells are studied. Spin coating and hydrolyzing of the precursor results in layers with an amorphous structure exhibiting oxygen deficiencies, hence the denotation  $\text{TiO}_x$ <sup>[78]</sup>. The theta-2theta scan of the as prepared  $\text{TiO}_x$  film, depicted in Figure 16, presents broad features at angles around  $27^\circ$ ,  $43^\circ$  and  $64^\circ$  indicating an amorphous structure as expected. To conclude that the sol-gel synthesis was successful and  $\text{TiO}_x$  was formed, the film was sintered at  $500^\circ\text{C}$  under ambient conditions. The repeated XRD measurement on the sintered film presents distinct diffraction features with peaks at  $25.5^\circ$ ,  $38.2^\circ$ ,  $48.0^\circ$ ,  $54.8^\circ$ ,  $63^\circ$ ,  $69.6^\circ$  and  $75.7^\circ$ , which can be assigned to the anatase crystalline structure of  $\text{TiO}_2$  according to the ICDD database. The sol-

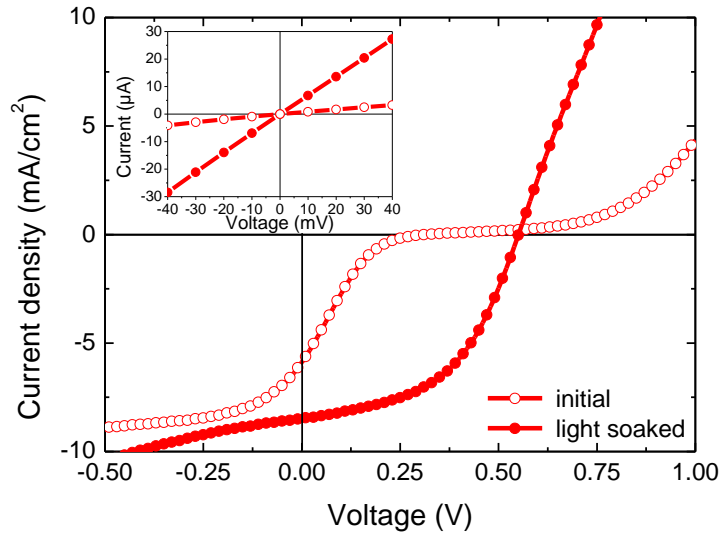


**Figure 16:** IV characteristics with initial solar cell parameters of  $j_{sc} = 5.86 \text{ mA cm}^{-2}$ ,  $V_{oc} = 0.32 \text{ V}$ ,  $\text{FF} = 14.7 \%$  and  $\text{PCE} = 0.27 \%$ , which increase to  $j_{sc} = 8.50 \text{ mA cm}^{-2}$ ,  $V_{oc} = 0.55 \text{ V}$ ,  $\text{FF} = 49.7 \%$  and  $\text{PCE} = 2.33 \%$  after light soaking. The inset shows the zero crossing of the dark IV characteristic before and after light soaking. Device resistances of  $R_{p,\text{initial}} = 10.9 \text{ k}\Omega$  and  $R_{p,\text{lightsoaked}} = 1.4 \text{ k}\Omega$  were extracted from the data.

gel synthesis produced the expected  $\text{TiO}_x$ , which was also investigated using an atomic force microscope, in order to probe the surface topography. Spin coating of the  $\text{TiO}_x$  precursor resulted in a smooth surface with a roughness (RMS) of 2.2 nm, suitable for use as the electron extraction layer in inverted solar cells as shown in the micrograph in Figure 16.

For the electrical characterization an exemplary solar cell was chosen, which initially presents an s-shaped IV curve, leading to a low fill factor of around 15 %. After light soaking for 20 minutes under illumination from a solar simulator the s-shape disappears and the fill factor equals approximately 50 % (Figure 17).

Impedance spectroscopy was used to gain a detailed insight into changes of the dielectric response of the solar cell before and after light soaking. Figure 18 shows the Cole-Cole plot of the impedance data for the solar cell before (open circles) and after (closed circles) light soaking. The inset shows the data obtained from the high to low frequency range (1 MHz – 100 Hz) while the larger graph contains the

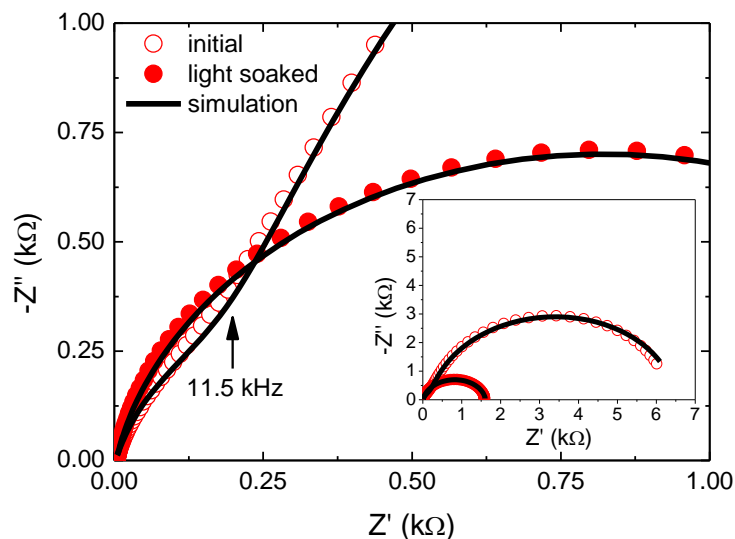


**Figure 17:** Cole-Cole representation of the high frequency range of the impedance data before (open circles) and after (closed circles) light soaking. The solid lines represent the simulated data from the fit using the circuit model in Figure 20 and the values in Table 3. The inset shows the entire frequency range of the data from 1 MHz – 100 Hz.

data obtained from the higher frequency range. Before light soaking the Cole-Cole plot clearly consists of two arcs with a transition frequency of 11.5 kHz, and the intersection of the low frequency arc with the x-axis corresponds to a total dc device resistance of 6.5 k $\Omega$ . After light soaking, the high frequency feature disappears and the dc resistance of the device decreases to 1.5 k $\Omega$ .

The frequency dependence of the capacitance (blue squares) and the dielectric loss (red circles) of the solar cell are shown in Figure 19 before (open symbols) and after light soaking (closed symbols). Before light soaking an increase in the capacitance at 11.5 kHz resulting in a plateau at lower frequencies is observed. The loss spectrum reveals a change in slope at the same frequency, resulting in a broad peak in the spectrum. This behavior is characteristic of systems with dominant interface or space charge effects, as trapped charge in the device increases the capacitance and the loss peak results from the slower reorientation of the trapped charge compared to mobile charge, leading to an energy loss<sup>[79]</sup>.

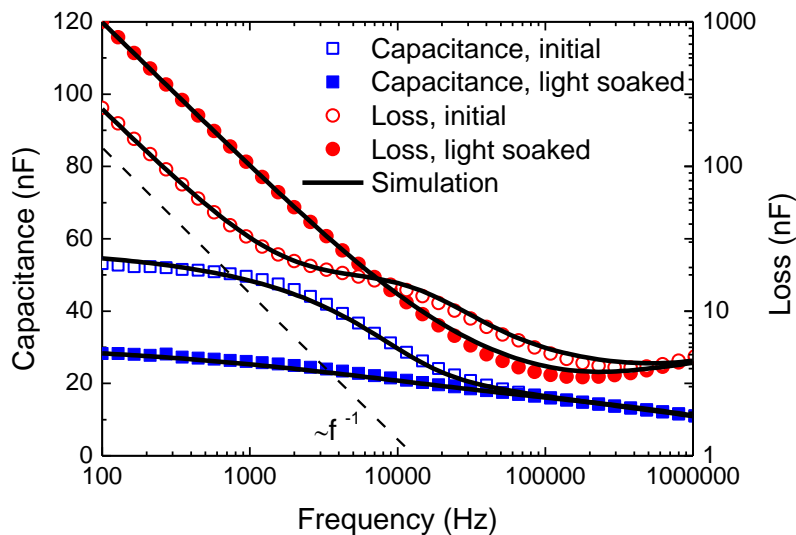


**Figure 18:** Capacitance (blue squares) and dielectric loss (red circles) spectra of the solar cell before (open symbols) and after (closed symbols) light soaking. The solid lines represent the simulated data from the fit using the circuit model in Figure 20 and the values in Table 3.

The change in the IV characteristics, in particular the FF, and the dielectric behavior of the device are expected to be a result of the change in the resistance of the  $\text{TiO}_x$  layer due to light soaking. Thus the change in resistance of a  $\text{TiO}_x$  layer is investigated over a period of 20 minutes during light soaking. The resistance of the  $\text{TiO}_x$  was measured independently by coating  $\text{TiO}_x$  on a substrate with interdigitated ITO electrodes. Using the relation  $\sigma = (I/V) * (d/A)$ , with  $d = 80 \mu\text{m}$  as the channel width and  $A$  as the area given by the channel length  $l = 0.75 \text{ m}$  times the thickness of the  $\text{TiO}_x$  interlayer  $t = 8.2 \text{ nm}$ . The obtained conductivity was then used to calculate the resistance of the  $\text{TiO}_x$  interlayer in the solar cell following  $R = (1/\sigma) * (t'/A')$  accounting the geometry of the solar cell with an active area  $A' = 0.5 \text{ cm}^2$  and a  $\text{TiO}_x$  thickness of  $t' = 3.3 \text{ nm}$ .

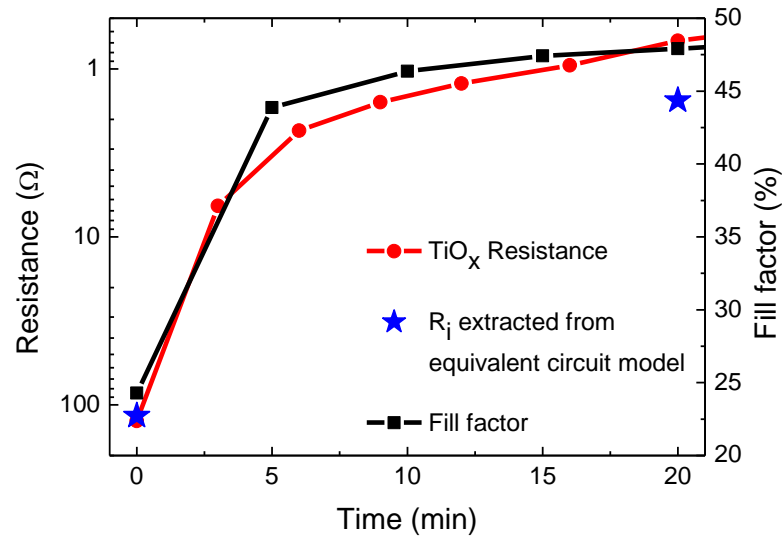


**Figure 19: Resistance of the  $\text{TiO}_x$  interlayer and fill factor of the according device in dependence of light soaking time.  $R_i$  values extracted from simulations of the equivalent circuit model shown in Figure 20 are included for comparison.**

Figure 20 shows the resistance of the  $\text{TiO}_x$  interlayer and the fill factor of the solar cell as a function of light soaking time. The trend followed by the resistance of the  $\text{TiO}_x$  interlayer and the FF of the solar cell is similar, indicating that the resistance of the  $\text{TiO}_x$  layer directly impacts the FF and therefore the shape of the IV charac-

teristics of the solar cell. Hence, an equivalent circuit model is proposed to describe the behavior of the solar cell before and after light soaking. This allows one to attribute the formation of an s-shape to changes in the circuit element attributed to the  $\text{TiO}_x$  layer, which additionally influences transport phenomena in the bulk.

Figure 21 presents the equivalent circuit diagram which was used to quantify the impedance data and describe the shape of the IV curves. The equivalent circuit model layout is designed to account for the different layers in the solar cell stack and simultaneously offers a very simplistic approach to investigate layers and interfaces in the solar cell. The model was used to fit the experimental Cole-Cole (Figure 18) and capacitance vs. frequency and dielectric loss vs. frequency (Figure 19) data before and after light soaking the solar cell. Changes in the IV curve of the solar cell due to light soaking are accounted for by changes in the values of the circuit elements of the model, indicating that the circuit model is accurate in quantitatively describing the behaviour of the solar cell, in particular the emergence and disappearance of the s-shape in the IV characteristics.

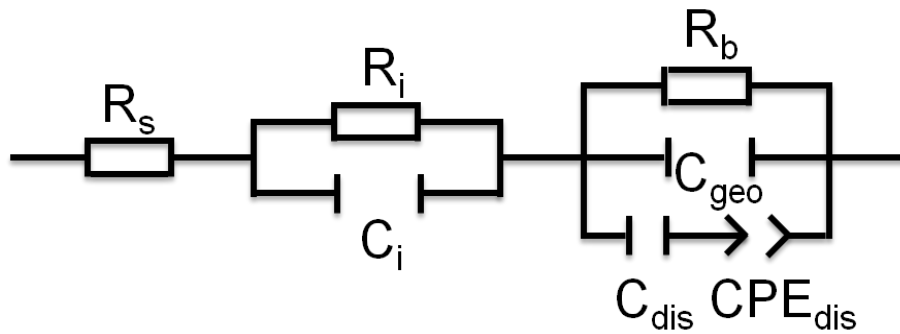


**Figure 20: Equivalent circuit model used to simulate the experimental data from the solar cell before and after light soaking.  $R_s$  – lead resistance;  $R_i$  and  $C_i$  – RC element to account for the  $\text{TiO}_x$  interlayer;  $R_b$ ,  $C_{geo}$ ,  $C_{dis}$ ,  $CPE_{dis}$  – compound circuit element to account for dispersive transport in the organic bulk.**

The equivalent circuit is composed of a lead resistance  $R_s$  to account for contact resistances.  $R_s$  was fixed at  $2.8 \Omega$  for simulations. An R-C element ( $R_i$ ,  $C_i$ ) is used to account for the  $\text{TiO}_x$  layer, the values of  $R_i$  and  $C_i$  were determined from fits of the experimental data before and after light soaking. A final compound circuit element is used to describe the dispersive transport in the polymer:fullerene active layer as described in chapter 2.4.  $R_b$  was determined from fits of the experimental data.  $C_{\text{geo}}$  was extracted from the negative bias regime of capacitance-voltage measurements of solar cells after light soaking. The value of  $C_{\text{geo}}$  was kept fixed at 11 nF for the simulations.

The values of the circuit elements before and after light soaking are listed in Table 3. The change in the IV curves after light soaking corresponds to changes in the RC element ascribed to the  $\text{TiO}_x$  interlayer ( $R_i$ ,  $C_i$ ), to changes in the bulk resistance ( $R_b$ ) and to changes in the constant phase element values ( $C_{\text{dis}}$  and CPE- $T_{\text{dis}}$ ).

**Table 3: Equivalent circuit parameters used to simulate experimental impedance spectroscopy data.**

	$R_s$ ( $\Omega$ )	$R_i$ ( $\Omega$ )	$C_i$ (nF)	$R_b$ (k $\Omega$ )	$C_{\text{geo}}$ (nF)	$C_{\text{dis}}$ (nF)	CPE- $T_{\text{dis}}$ ( $\mu$ F)	CPE- $P_{\text{dis}}$
initial	2.8	116.3	57.2	6.3	11	48.8	12	0.52
light soaked	2.8	1.54	110.3	1.6	11	20.2	1.3	0.62

The decrease in  $R_i$  and  $C_i$  after light soaking can be explained by the mechanism causing the change in  $\text{TiO}_x$  resistance due to light soaking<sup>[80]</sup>. Upon UV irradiation, oxygen is released from the  $\text{TiO}_x$ . This results in an increase of the density of mobile electrons in the layer, as well as of positively charged vacancies. This results in both a decrease in the resistance of the material due to conducting charges as well as an increase in capacitance due to the trapped charges. The capacitance increases from 57.2 nF to 110.3 nF and simultaneously the resistance  $R_i$  decreases from 116.3  $\Omega$  to 1.54  $\Omega$  after light soaking.

The  $R_i$  values from the model can be compared to the measured resistance of the  $\text{TiO}_x$  interlayer, discussed in the previous section. Measuring the resistance of the  $\text{TiO}_x$  interlayer taken before and after 20 min of light soaking (resistance values are shown as stars in Figure 20), values of  $R_{\text{TiO}_x, \text{initial}} = 124.7 \Omega$  and  $R_{\text{TiO}_x, \text{lightsoaked}} = 0.68 \Omega$  are found, before and after light soaking, respectively. These experimental values are in good agreement with the values for  $R_i$  from the equivalent circuit model.

Before light soaking, the highly resistive  $\text{TiO}_x$  layer is expected to inhibit efficient extraction of charge carriers from the solar cell, resulting in an s-shape in the IV characteristics<sup>[72]–[76]</sup>. The unbalanced extraction of charge can lead to space charge effects in the bulk. This is demonstrated by the initially high values of  $R_b$ ,  $C_{\text{dis}}$  and  $\text{CPE-T}_{\text{dis}}$ , which then collectively decrease after light soaking. The values of  $R_b$  dominate the total device resistance, and correspond well with the values extracted from the dark IV characteristics (shown in the inset of Figure 17). Initially, the total device resistance is 10.9 k $\Omega$ , and drops to 1.4 k $\Omega$  after light soaking, which agrees with the change in the values of  $R_b$  of 6.3 k $\Omega$  and 1.6 k $\Omega$  before and after light soaking, respectively. The capacitance of the bulk depends on the efficiency of charge transport out of the active layer, which is inhibited by the  $\text{TiO}_x$  before light soaking.

The equivalent circuit model analysis proposed here, presents a possible method to diagnose loss mechanisms in organic solar cells. Using a model system based on a  $\text{TiO}_x$  interlayer with variable resistance, the robustness of the technique could be demonstrated. Hence, this method can be applied generally, to investigate degradation mechanisms and stability issues in solar cells.

## 4.2 The influence of the hole transport layer on solar cell performance and stability<sup>2</sup>

In this chapter the influence of the hole transport layer on device stability is investigated. Water can have significant influences on the stability of organic solar cells and can lead to drastic reductions in power conversion efficiencies. The influence of the polymer and the solvent used to fabricate the dispersion for the hole transport layer material is studied. The widely used water based PEDOT:PSS is compared to novel hole extraction layers based on PANI:PSS, which are either dissolved in water or in alcohol. In literature only a few publications deal with the investigation of degradation mechanisms related to the anode and the hole extraction layer. Although a variety of oxides, like WO<sub>3</sub>, MoO<sub>3</sub> or V<sub>2</sub>O<sub>5</sub> or organic materials, like PANI or PANI:PSS were used as hole transport layers in either organic light emitting diodes or organic solar cells, these investigations were mostly conducted in terms of considering the improvements in efficiency achieved using different transport layers rather than studying the effect on the stability of the device<sup>[81]–[86]</sup>.

Jong et al.<sup>[87]</sup> showed that PEDOT:PSS, having a pH value between 1 and 2, etches indium out of the ITO anode leading to the incorporation of indium in the active layer which can be responsible for a decreased life time. Kawano et al.<sup>[88]</sup> investigated the influence of air and humidity on ITO/PEDOT:PSS/MDMO-PPV:PCBM/Al solar cells, showing that the hygroscopic nature of PEDOT:PSS can be a significant degradation mechanism in organic solar cells. Inverted solar cells recently showed a remarkably higher stability in comparison with organic solar cells in the standard structure, mostly due to the use of a high work function

---

<sup>2</sup> Parts of the results presented in this chapter are published in B. Ecker et al. *Adv. Funct. Mater.* (2011) **21**, 2705-2711, DOI: 10.1002/adfm.201100429.

metal anode, which is less sensitive to degradation than low work function metals used as cathodes in non-inverted solar cells<sup>[89]-[91]</sup>. However, PEDOT:PSS is still incorporated in inverted solar cells as hole extraction layer between the active layer the high work function anode. Norrman et al.<sup>[92]</sup> identified the PEDOT:PSS layer as one of the main degradation sites in inverted solar cells via time-of-flight secondary ion mass spectrometry together with isotopic labeling of oxygen and

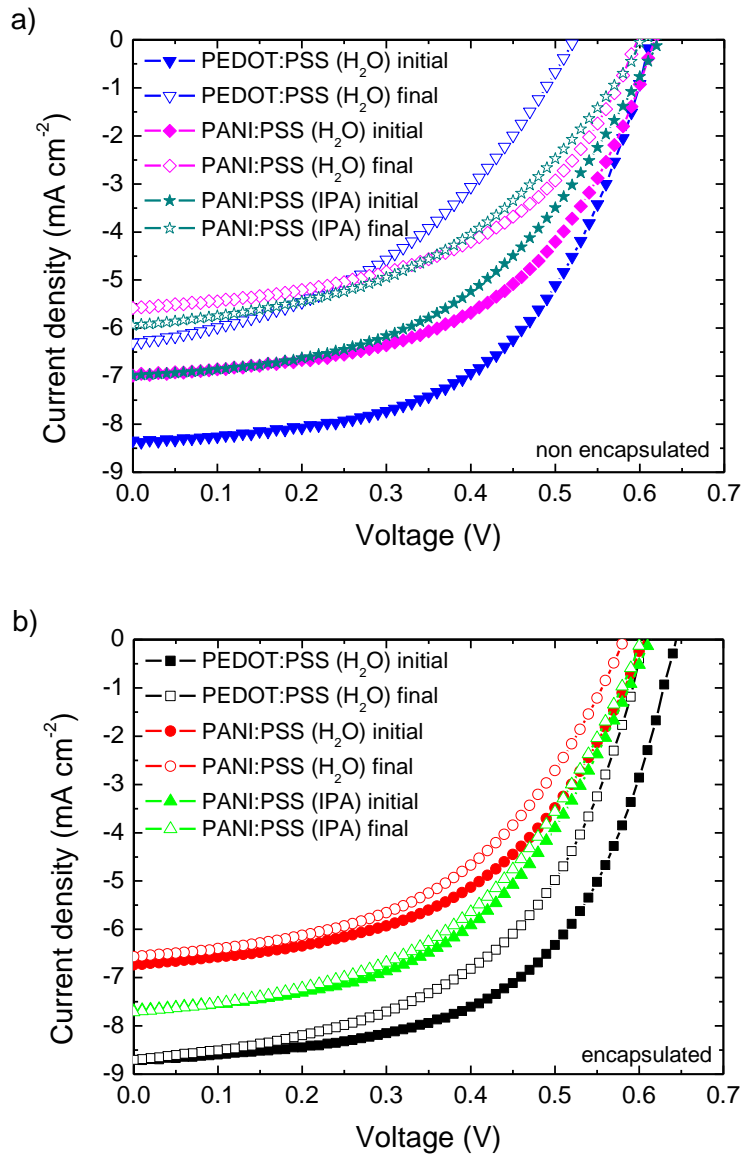


**Figure 21: Current density-voltage characteristics of a) non encapsulated and b) encapsulated solar cells with different hole transport layers at initial and final conditions.**

water. Finding a substitute for PEDOT:PSS is necessary, in order to increase the lifetime of organic solar cells.

Solar cells in the structure ITO/HTL/P3HT:PCBM/Ca/Al are prepared, as depicted in Figure 13a). A blend of P3HT:PCBM was used as the active layer and three different hole transport layers were investigated, two water based formulations, PEDOT:PSS (H<sub>2</sub>O) and PANI:PSS (H<sub>2</sub>O), and one isopropyl alcohol based PANI:PSS (IPA). The hole transport layers additionally differed from each other in composition, conductivity and work function, due to different precursor solutions. The characteristics of the hole transport layers are summarized in Table 1.

By varying only the hole transport layer between the devices it is possible to isolate the degradation effects related specifically to the hole transport layer interface in the device. Additionally, the characteristics of non-encapsulated and encapsulated cells are compared in order to gain insight into the difference between internal (residuals of solvent, water, oxygen in the encapsulated solar cell) and external (influences of ambient air and humidity) degradation mechanisms at the hole transport layer interface.

To investigate the solar cells, IV, capacitance-voltage (CV) and capacitance-frequency (Cf) characteristics were measured under different illumination intensities. Fresh solar cells were measured initially under 1 sun, and subsequent measurements were performed under increasing light intensities, at 16, 30, 48, 80, and 100 mW cm<sup>-2</sup>. The solar cells were under illumination for a total of 7 hours. In Figure 22 the initial and final IV characteristics of the solar cells at 100 mW cm<sup>-2</sup> for the non-encapsulated cells (a) and the encapsulated cells (b) are shown. The corresponding solar cell parameters are summarized in Figure 23.

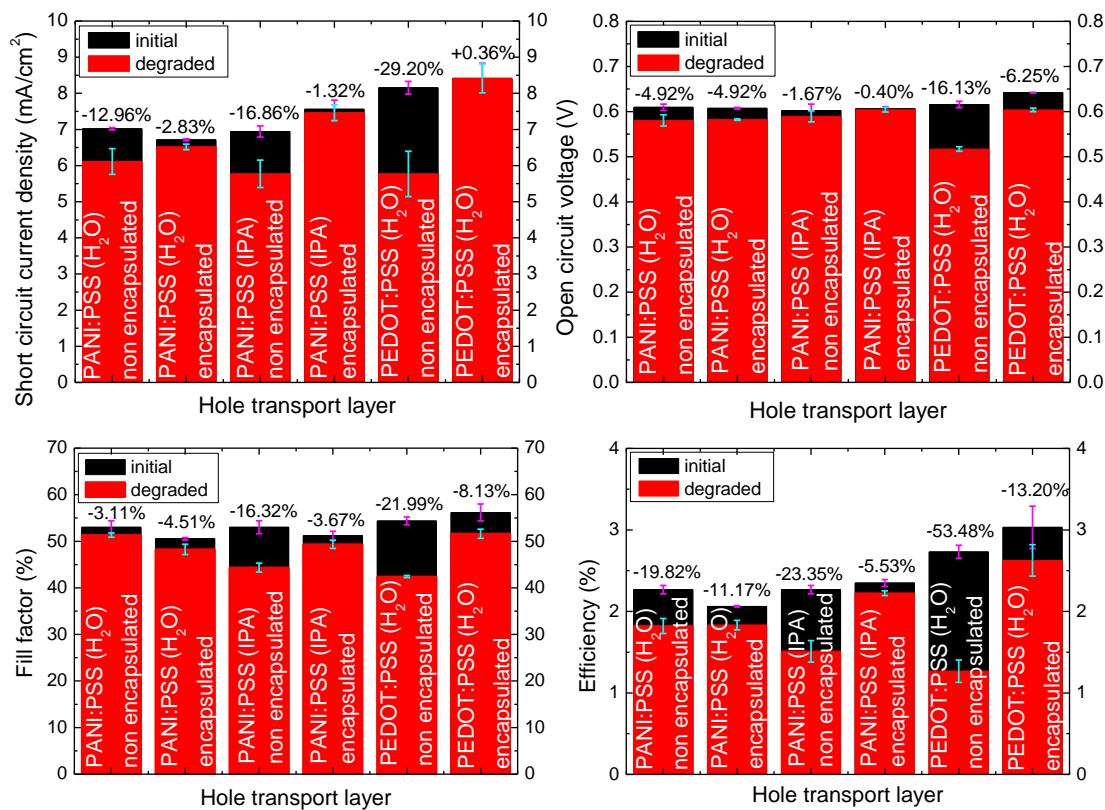
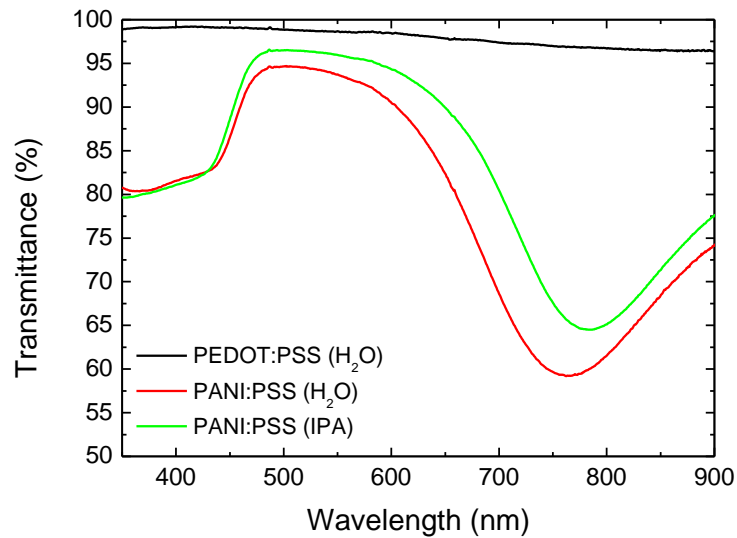


Figure 22: Solar cell parameters of the solar cells shown in Figure 22 together with the loss due to degradation over 7 hours under increasing light intensity in percent.

The cells prepared with PEDOT:PSS (H<sub>2</sub>O) initially demonstrated the best performance. This is attributed to the difference in transmittance of the hole transport layers shown in Figure 24. The PEDOT:PSS layer has a higher transmittance compared to the PANI:PSS layer based solar cells, allowing for more light absorption by the active layer and therefore an increase in the photo-generation of charge, leading to a higher short circuit current density ( $j_{sc}$ ). Although the work functions of the hole transport layers vary between 4.81 eV (PEDOT:PSS (H<sub>2</sub>O)) and 5.49 eV (PANI:PSS (IPA)) the open circuit voltages ( $V_{oc}$ ) of the fresh cells are comparable. This is attributed to the pinning of the work function of the hole

transport layer to the highest occupied molecular orbital (HOMO) of the polymer<sup>[45]</sup>.

From the comparison between the initial and final measurements it can be seen that a decrease in the solar cell performance occurs for both encapsulated and non-encapsulated devices (Figure 23). In the case of the non-encapsulated devices,  $j_{sc}$  is significantly diminished between the initial and final measurements in all devices.



**Figure 23: Transmittance spectra of the hole transport layers investigated using the same preparation conditions as used for the solar cells. Film thicknesses were 35 nm for PEDOT:PSS (H<sub>2</sub>O), 63 nm for PANI:PSS (H<sub>2</sub>O) and 121 nm for PANI:PSS (IPA).**

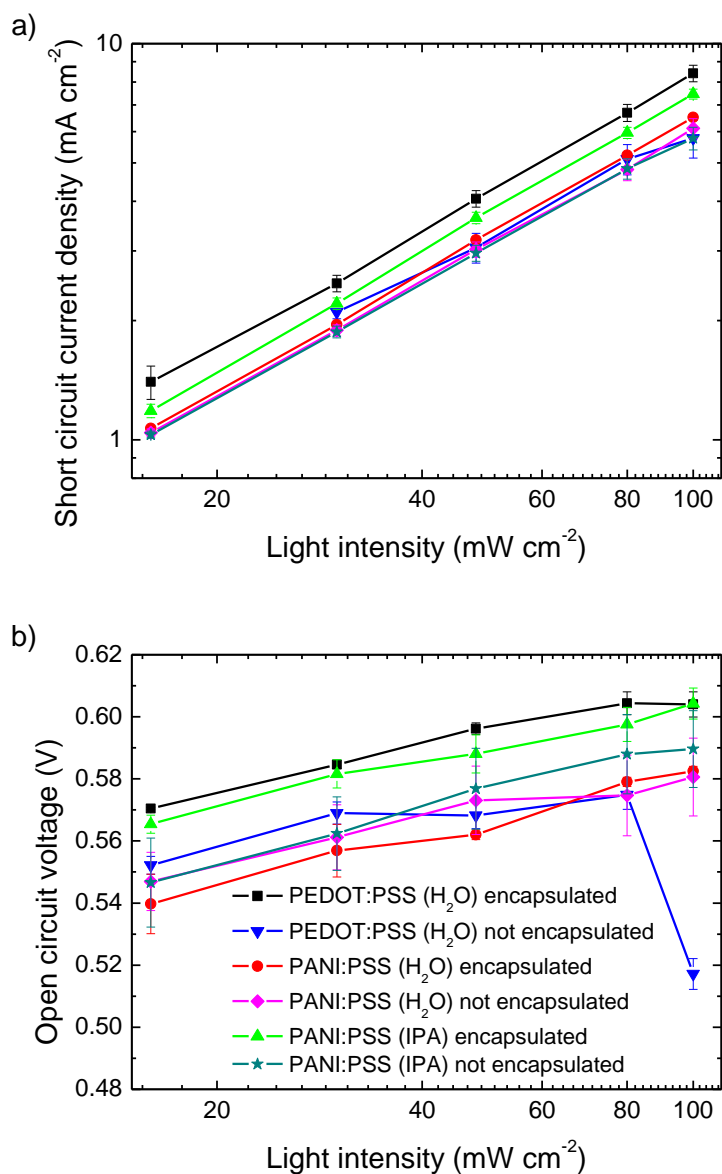


**Figure 24:** a) Short circuit current density ( $j_{sc}$ ) and b) open circuit voltage ( $V_{oc}$ ) of the solar cells presented in Figure 21 plotted versus light intensity. A clear deviation of  $V_{oc}$  of the non-encapsulated device from the logarithmic behaviour with increasing light intensity can be observed.

Additionally, there is a decrease in the fill factor of the devices, and in the case of PEDOT:PSS (H<sub>2</sub>O) the  $V_{oc}$  is considerably lower after degradation. In general, taking into account the power conversion efficiency one can clearly observe a

more than doubled reduction of the efficiency for the non-encapsulated PEDOT:PSS (H<sub>2</sub>O) in contrast to the non-encapsulated PANI:PSS based solar cells. This implies that the extrinsic stability of the PANI:PSS is much higher than that of PEDOT:PSS. Additionally for the encapsulated devices the reduction in efficiency is again doubled for the water based hole transport layers in contrast to the isopropyl alcohol based PANI:PSS solar cell, indicating that residual water from the hole transport layers can degrade the encapsulated solar cells. This means that by using an IPA-based hole transport layer PANI:PSS the intrinsic stability of organic solar cells can be improved. Figure 25 presents mean  $j_{sc}$  (a) and  $V_{oc}$  (b) values versus light intensity data and the standard deviation for all of the non-encapsulated and encapsulated solar cells investigated. The  $j_{sc}$  shows a power law dependence on the illumination intensity ( $P_{light}$ )  $j_{sc}=P_{light}^{\alpha}$ , with  $\alpha \sim 1$ <sup>[93],[94]</sup>. The  $V_{oc}$  varies linearly with the logarithm of the illumination intensity, except for the non-encapsulated PEDOT:PSS (H<sub>2</sub>O) containing device, where the decrease in  $V_{oc}$  due to degradation is apparent<sup>[93],[95]</sup>.

To obtain deeper insight into the processes involved in the degradation associated with the hole transport layer, impedance spectroscopy was used to investigate the light intensity dependent capacitance-voltage (CV) and capacitance-frequency (Cf) characteristics of the solar cells. In inorganic crystalline materials impedance spectroscopy can be used to probe defect states in the band gap<sup>[96]</sup>. As already discussed in chapter 2.1, Monroe has demonstrated that hopping transport in disordered organic semiconductors is mathematically equivalent to band transport with multiple trapping and release processes and that the transport energy ( $E_T$ ) equates the specific energy range at which the hopping rate is maximized<sup>[35]</sup>. This transport energy is consistent to the mobility edge separating the localized and delocalized states<sup>[35]</sup>. Hence, in the case of disordered organic semiconductors, impedance spectroscopy can be applied to probe the energetic disorder of transport sites in the material.

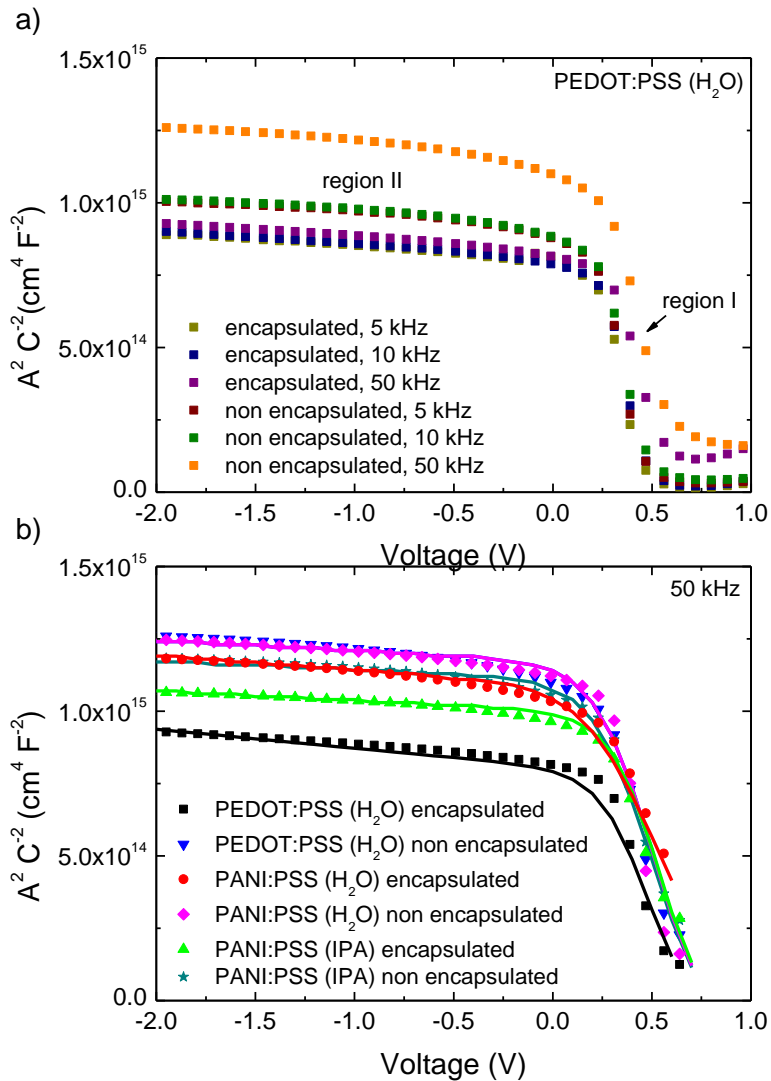


**Figure 25:** a) Mott-Schottky representation of experimental capacitance-voltage data (symbols) measured in the dark of encapsulated and non-encapsulated devices containing PEDOT:PSS (H<sub>2</sub>O) as hole transport layer, b) simulations (lines) compared to experimental data (symbols) of the different hole transport layers at an applied frequency of 50 kHz.

In Figure 26a) the CV characteristics of the PEDOT:PSS (H<sub>2</sub>O) based device conducted in the dark at frequencies of 5kHz, 10kHz and 50 kHz are shown in the Mott-Schottky representation. Two regimes with different slopes can be observed from the characteristics, one (I) at around 0 V to +0.5 V and the second (II) at -2 V to 0 V. These regimes are related to the profile of the space charge in the device in inorganic junctions and have been attributed to the contributions from the donor

phase (I) and the acceptor phase (II) in organic solar cells<sup>[97],[98]</sup>. Probing the capacitance vs. voltage over different frequencies demonstrates that the slopes in both regions I and II remain constant but a shift in the characteristics with increasing frequencies to higher forward voltages can be observed. This implies that the built-in voltages, which are given by the extrapolated interception of the respective region with the voltage axis, depend on the frequency applied during the measurement, an indication that interface traps are present<sup>[99],[100]</sup>.

The charge carrier concentration from region I (P3HT)  $N_{P3HT}$ , can be extracted referring to the classical abrupt junction model using the standard Mott-Schottky analysis, under the assumption that  $N_{PCBM} \gg N_{P3HT}$ <sup>[99],[101]</sup>:

$$\left(\frac{A}{C}\right)^2 = \frac{2 \cdot (V - V_{Bi})}{q \cdot \epsilon_0 \cdot \epsilon_r \cdot N_A} \quad (8)$$

, where  $A$  is the active area of the solar cell,  $C$  is the capacitance,  $V$  is the applied voltage,  $V_{Bi}$  is the built-in voltage,  $q$  is the elementary charge,  $\epsilon_0$  is the vacuum permittivity,  $\epsilon_r$  is the relative dielectric constant of the material under test and  $N_A$  is the doping concentration.

Applying equation (8) to the CV characteristics recorded at 50 kHz for the various illumination intensities the charge carrier concentration is obtained in the P3HT phase vs. light intensity shown in Figure 27a). In order to calculate the charge carrier concentration in the PCBM phase  $N_{PCBM}$  (region II), it is assumed that the P3HT phase is fully depleted of free charges, and the following relation was used<sup>[97],[100]</sup>:

$$V_{II} = V_{Bi} + \left(\frac{q}{2 \cdot \epsilon_r \cdot \epsilon_{PCBM}}\right) \cdot N_{PCBM} \cdot t^2 \quad (9)$$

, where  $V_{II}$  is the intercept of region II with the voltage axis,  $\epsilon_{PCBM}$  is the relative dielectric constant of PCBM and  $t$  is the thickness of the P3HT phase. The calculated charge carrier concentration of the PCBM phase vs. light intensity is shown in Figure 27b).

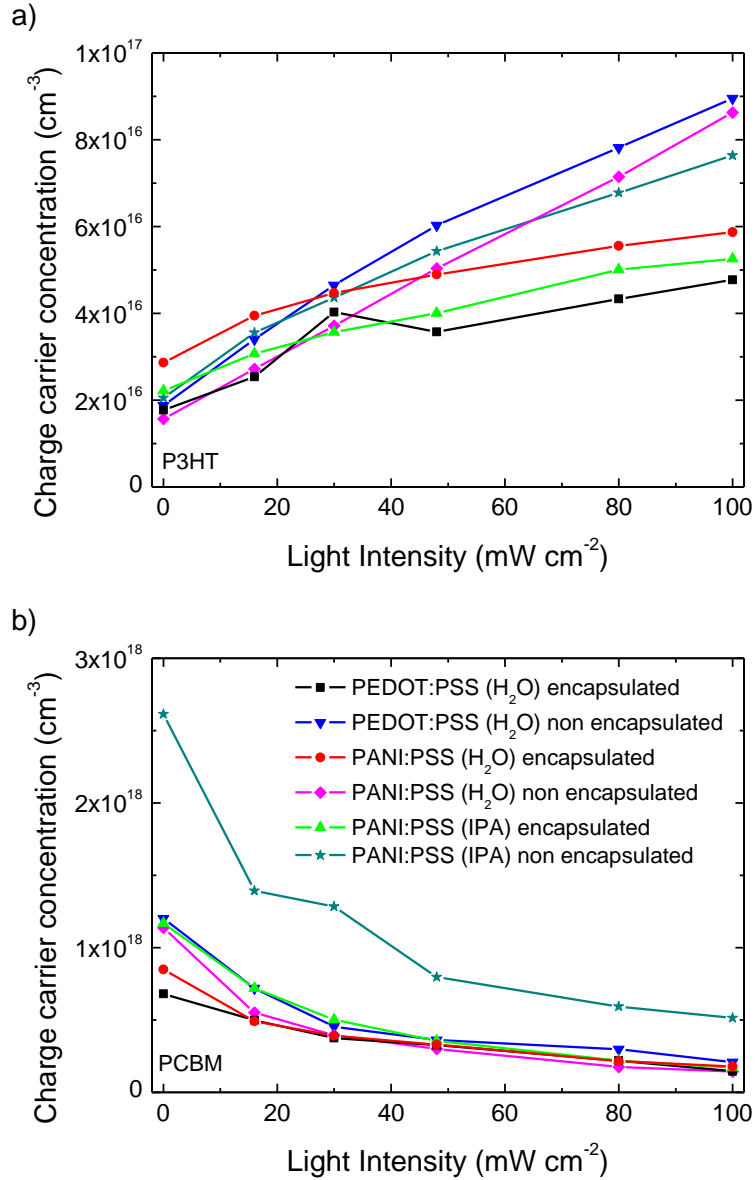


**Figure 26: Charge carrier concentration in a) P3HT and b) PCBM plotted versus illumination intensity. Values extracted from CV measurements taken at 50 kHz.**

The extracted free charge carrier concentrations of P3HT and PCBM were used in AFORSHET V2.2 to simulate CV data. The simulated data (lines) is presented together with the experimental data for the CV characteristics (symbols) at 50 kHz in Figure 26b) and demonstrate good agreement. An error in the sample thickness of 15 nm and in the charge carrier concentration of  $4 \times 10^{15} \text{ cm}^{-3}$  was found.

In the case of P3HT it can be seen that the charge carrier concentration increases with light intensity for all the devices, as expected for the photo-generation of charges in the bulk. There is an increase in the slope of the characteristics in the non encapsulated devices compared to the encapsulated devices. This is attributed to oxygen doping, which introduces trap states for electrons into the bulk<sup>[15]</sup>. This can result in an increase in the hole density in the polymer. In the case of PCBM, there is a slight decrease observed in the charge carrier concentration with increasing illumination intensity and degradation time for all devices. This could be due to increased oxidation of the polymer or fullerene with degradation time<sup>[63],[102]</sup>. A decrease of the charge carrier concentration in the acceptor phase has also been observed in degraded solar cells with a copper phthalocyanine (CuPc) : N,N'-bis(2-phenylethyl)-perylene-3,4,9,10-tetracarboxylic diimide (BPE-PTCDI) heterojunction<sup>[101]</sup>.

Using Cf measurements the density of states (DOS) was calculated as proposed by Walter et al.<sup>[96]</sup> for non-crystalline, inorganic materials, which was recently applied by Reis et al.<sup>[103]</sup> for polymer diodes and by Boix et al.<sup>[104]</sup> for polymer:fullerene solar cells applying:

$$DOS(E) = -\frac{V_{Bi} \cdot \omega}{t \cdot q \cdot k_B \cdot T} \cdot \frac{dC}{d\omega} \quad (10)$$

, where  $E$  is the energy,  $V_{Bi}$  is the built-in voltage,  $\omega$  is the angular frequency,  $k_B$  is the Boltzmann factor and  $T$  is the temperature in Kelvin.

In inorganic semiconductors this model can be used to probe defect states within the band gap, as trapped charges contribute to the capacitance. Hence, one can translate this to the probing of energetic disordered transport sites in the organic material. The model by Walter et al.<sup>[96]</sup> assumes that the variation of the capacitance regarded to the angular frequency directly corresponds to trapping and release of charges in trap sites located around the Fermi energy  $E_F$ . In the case of disordered organic semiconductors, one can understand this to equate to probing transport sites close to  $E_F$  located energetically below the transport energy  $E_T$ .

The assumption in equation (10) is that variations in the capacitance of the device with frequency directly correspond to trapping and release of charge by trap sites in the band gap close to the Fermi energy ( $E_F$ ). In the case of disordered organic materials, one can translate this to probing transport sites close to  $E_F$  located energetically below  $E_T$ .

In order to translate the angular frequency dependent DOS into an energy dependent DOS<sup>[96]</sup>

$$E = k_B \cdot T \cdot \ln\left(\frac{2 \cdot \beta \cdot N}{\omega}\right) \quad (11)$$

is applied, where  $N$  denotes the effective density of states and  $\beta$  is the capture cross section.

In this study a value for  $\beta$  was assumed, which usually can be extracted from temperature dependent measurements. It should be noted that changes in  $\beta$  only result in a shift of the DOS on the energy scale, and not a change in the shape of the distribution. In the following, the influence of the different hole transport layers on the shape of the DOS is examined.

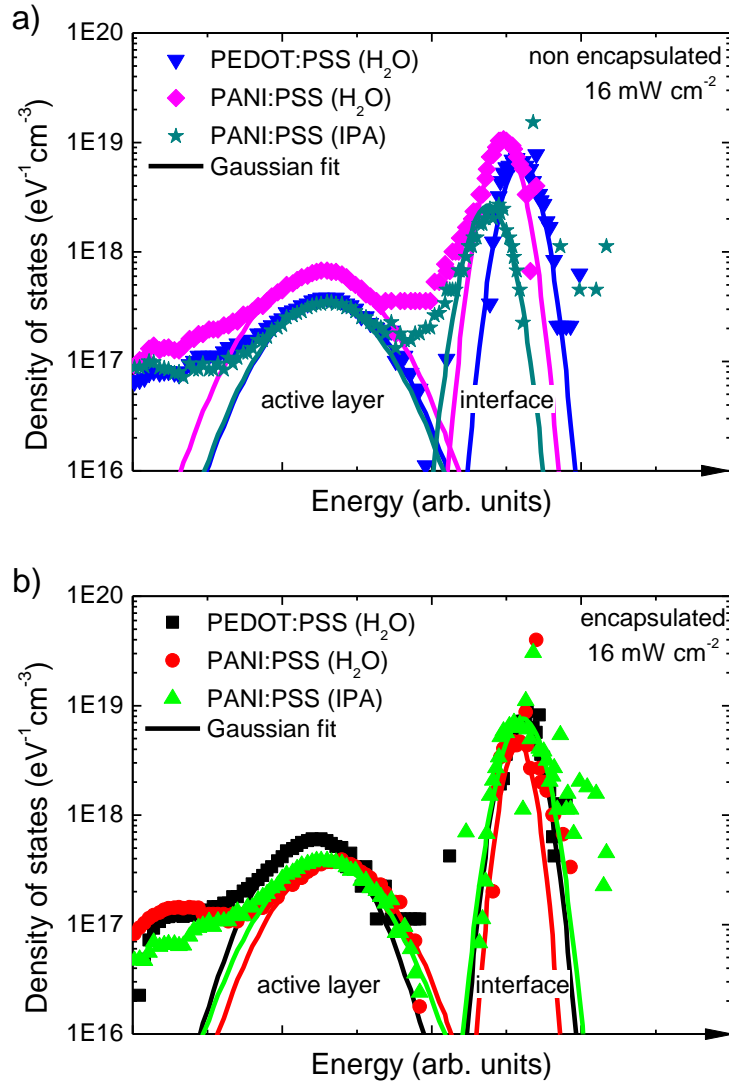


**Figure 27: Density of states (DOS) plotted vs. energy for a) non encapsulated and b) encapsulated devices illuminated with  $16 \text{ mW cm}^{-2}$  under open circuit conditions. Lines show Gaussian fits to states attributed to the bulk and interface.**

Figure 28 presents the calculated DOS at open circuit conditions at illumination intensities of  $16 \text{ mW cm}^{-2}$  at the start of the degradation process. Two Gaussian distributions at different energetic positions are present. The Gaussian at lower energies is attributed to the DOS in the active layer, as the distribution is common to all the devices.

From this analysis, it is not possible to distinguish between contributions from the electron and hole sites to the DOS<sup>[103]</sup>. The higher noise ratio for the distribution at higher energies is an indication that this distribution accounts for the hole transport layer interface as it also varies between the samples containing different hole transport layers and is accompanied by flicker noise<sup>[105]</sup>. The hole transport layers for both encapsulated and not encapsulated devices show a similar behavior at  $16 \text{ mW cm}^{-2}$ , as the devices are still fresh.

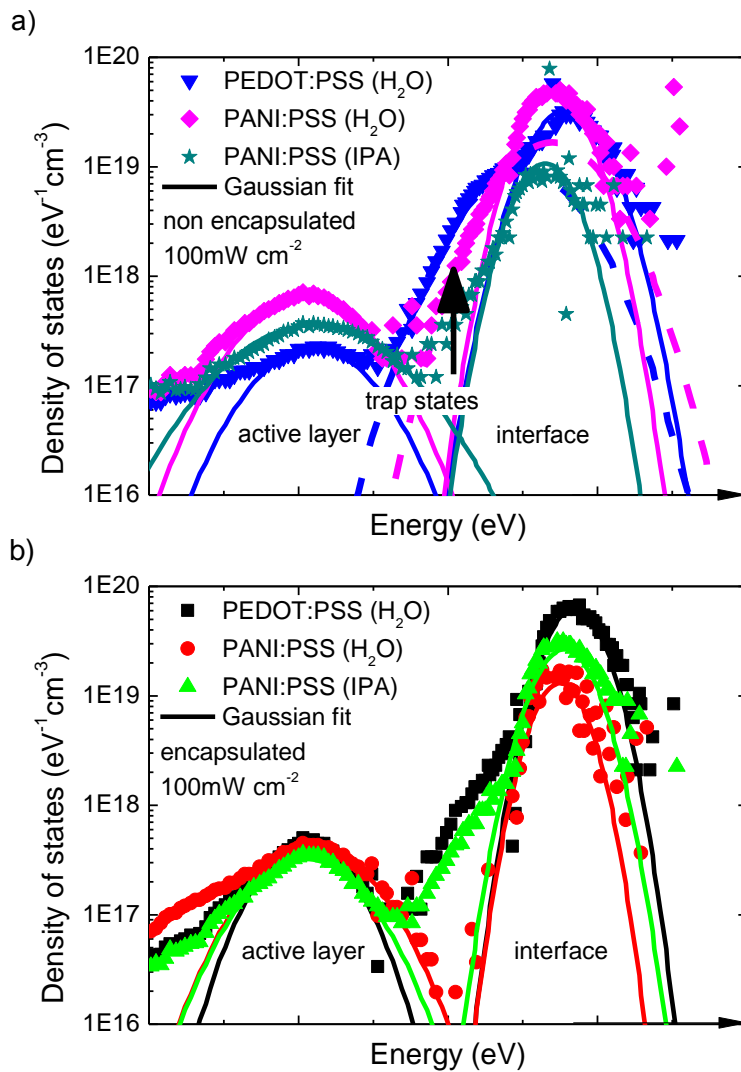


Figure 28: Density of states (DOS) plotted vs. energy for a) non encapsulated and b) encapsulated devices illuminated with  $100 \text{ mW cm}^{-2}$  under open circuit conditions. Lines show Gaussian fits to states attributed to the bulk and interface. Dashed lines are fits to states originating to interfacial trap states.

Figure 29 presents the DOS of solar cells after 7 hours of degradation under increasing light intensity for non encapsulated as well as encapsulated devices at  $100 \text{ mW cm}^{-2}$ . The Gaussian distribution related to the bulk is shifted towards slightly lower energies and a broadening of the distribution is observed. This effect is more apparent in the non encapsulated devices but also visible in the encapsulated devices. This effect may be due to the increase in charge carrier concentration at higher light intensities, leading to the filling of higher energy states. It may, however, also be a result of degradation, specifically of traps due to oxygen or humidity in the case of the non encapsulated devices in addition to internal instabilities in the bulk, such as changes to the morphology, for both non encapsulated and encapsulated devices.

The distribution related to the hole transport layer interface also demonstrates a broadening in form and the DOS is shifted away from the bulk related distribution to higher energies compared to the initial data at  $16 \text{ mW cm}^{-2}$ . Interestingly, in the case of the water based hole transport layers an additional shoulder becomes visible, which is prominent for the PEDOT:PSS ( $\text{H}_2\text{O}$ ) and also observed for the PANI:PSS ( $\text{H}_2\text{O}$ ). Additional Gaussian fits in this energy range reveal distributions, which are attributed to the formation of additional trap states at the interface between the hole transport layer and bulk. This is a clear indication that the choice of solvent of the hole transport layer has a major impact on device stability, which is improved with IPA based solvents over water based solvents.

Based on these results it is apparent that the properties of the hole transport layer can have a significant impact on the stability of organic solar cells. The effects of the hole transport layer properties (composition, solvent and work function) on the performance of the solar cell were investigated. It was seen that PEDOT:PSS ( $\text{H}_2\text{O}$ ) resulted in the best initial performance for the solar cells investigated here. This was attributed to the higher transmittance of the PEDOT:PSS ( $\text{H}_2\text{O}$ ). The work functions of the hole transport layers were not observed to influence the initial solar cell performance, due to the pinning of the Fermi level to the HOMO of

the polymer. The solvent of the hole transport layer was observed to have an effect on the device stability. The IPA based hole transport layer resulted in the most stable device, while the water based hole transport layers led to a more rapid deterioration in the solar cell performance.

### 4.3 The influence of the PSS content in PANI:PSS on the performance and stability of organic solar cells

In this chapter further investigations on the influence of the hole transport layer on the performance and stability in standard stacked organic solar cells are carried out. As already discussed in chapter 4.2 the acidic nature of PSS contained in hole transport layers is assumed to cause etching of indium and tin fractions of the ITO electrode which then diffuse throughout the device<sup>[87]</sup>. In this chapter PANI:PSS hole transport layers with different concentrations of PSS are studied in order to investigate the influence on the performance and stability of organic solar cells. Solar cells were prepared according the description in chapter 3.2 with either one of the hole transport layers summarized in Table 2 and encapsulated in order to neglect extrinsic influences (ambient air, humidity) on the device stability. Figure 30 presents the IV characteristics of the solar cells before and after degradation for 630 minutes under illumination. Initially, the solar cells with the hole transport layers with a lower PSS content show higher power conversion efficiencies.

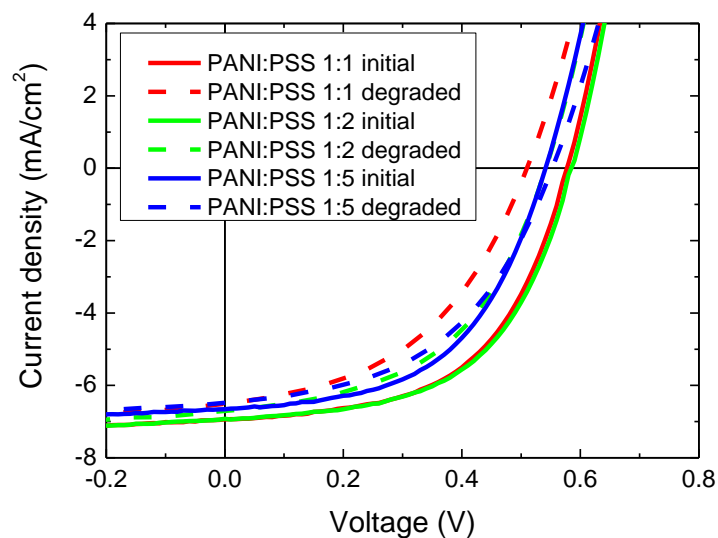


**Figure 29:** IV characteristics of encapsulated solar cells with PANI:PSS based hole transport layers with varying PSS content before and after degradation under illumination for 630 minutes.

As PSS is a transparent non-conductive material, further investigations on the correlation of the short circuit current density of the solar cell, with the transmission and the conductivity of the respective hole transport layers were carried out. Therefore, the different PANI:PSS formulations were spin coated onto structured ITO substrates. Using impedance spectroscopy, Cole-Cole plots were recorded, from which the respective conductivities could be calculated by taking into account the geometric dimensions of the structured ITO and the PANI:PSS film thickness.

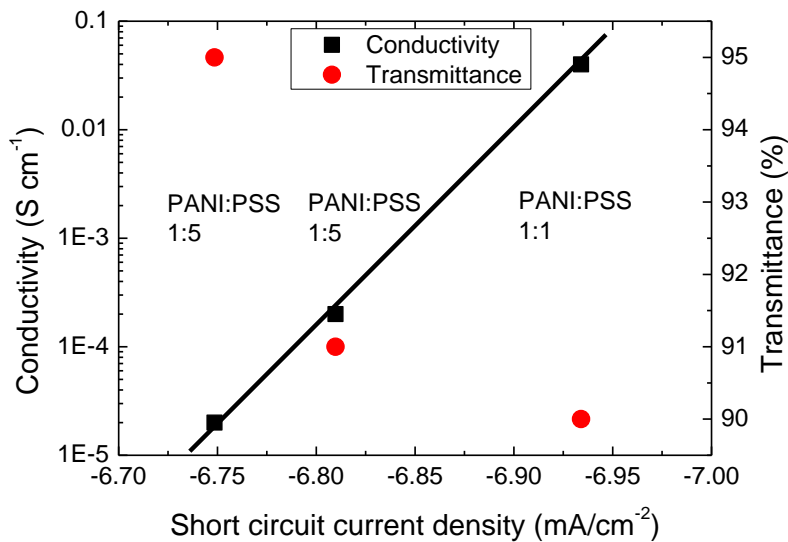
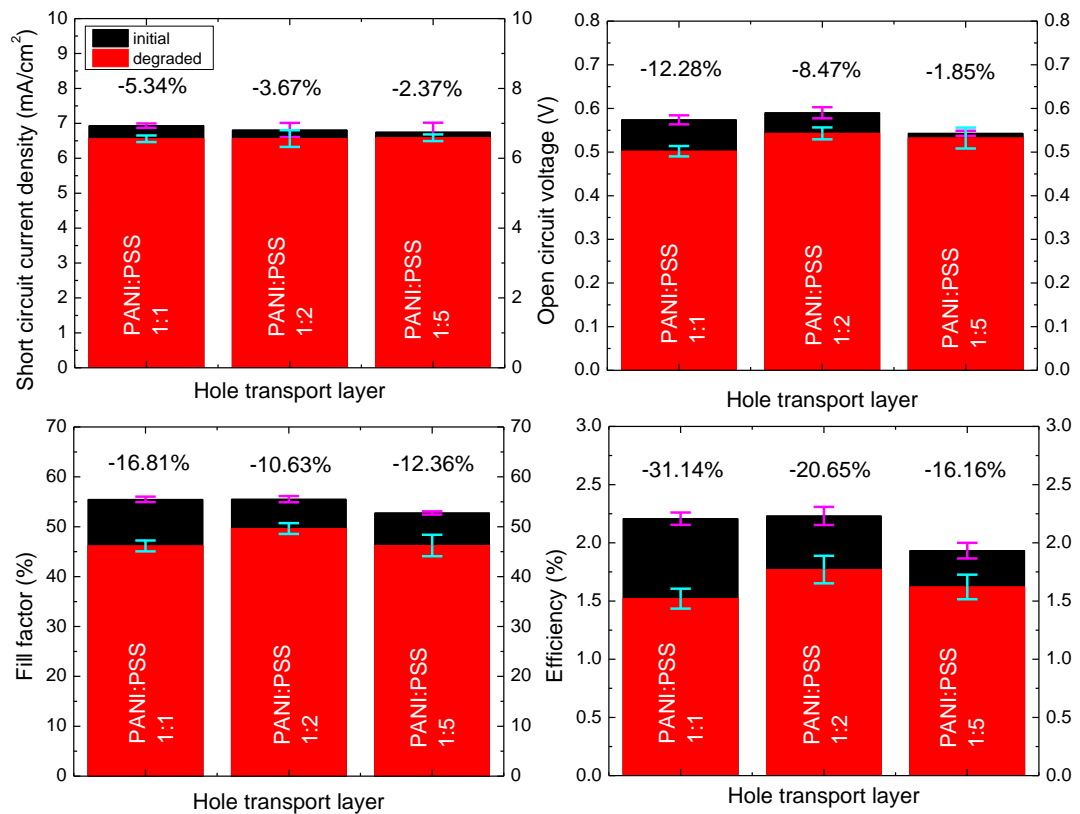


**Figure 30: Correlation between the short circuit current density ( $j_{sc}$ ) with conductivity and transmittance of the different hole transport layers.**

Figure 31 presents the conductivity and transmittance values of the hole transport layers, also summarized in Table 2, in correlation with the short circuit current densities in the respective solar cells. One can observe an increase in short circuit current density with an exponentially increasing conductivity. However, the effect of transmittance of the hole transport layer, which slightly increases with the incorporation of more PSS, is less pronounced, indicating that the conductivity of the hole transport layer has a stronger influence on the solar cell parameter than the transmittance. One can then conclude that in the case of fresh devices the solar

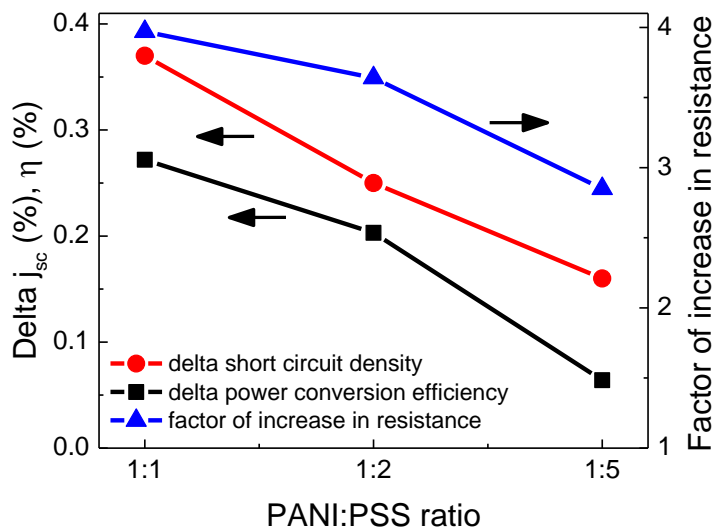
cell performance increases with decreasing PSS content related to an accompanied increase in hole transport layer conductivity.

Figure 32 presents mean values and standard deviations of the solar cell parameters extracted from IV characteristics of four devices for each hole transport layer before and after degradation. As already discussed, fresh solar cells incorporating a hole transport layer with low PSS content result in the highest short circuit current ( $j_{sc}$ ) and therefore show the highest efficiencies. Upon degradation of the devices under white light illumination (AM1.5G,  $100\text{mW cm}^{-2}$ ) for 630 minutes, all solar cell parameters show decreased values. However, concentrating on the short circuit current density and power conversion efficiency one can clearly observe, that the loss in performance decreases with increasing PSS content. The reduction



**Figure 31: Mean values and standard deviations of solar cell parameters before and after degradation of four devices for each hole transport layer including the solar cells presented in Figure 29.**

in short circuit current density and power conversion efficiency is more than doubled for the hole transport layer with a 1:1 ratio in contrast to the more stable hole transport layer with a 1:5 ratio. Hence, the amount of PSS in the hole transport layer has a strong influence on the stability of the devices. However, this is in contrast to the expected behaviour reported in literature, that PSS is responsible for the degradation of organic solar cells with PEDOT:PSS as hole transport layer<sup>[87]</sup>.



**Figure 32: Correlation of the increase in hole transport layer resistance with degradation to the change in short circuit current density and power conversion efficiency in solar cells with the respective hole transport layers.**

A strong influence of the conductivity of the hole transport layer on the solar cell performance is observed. Figure 33 thus presents the correlation of the hole transport layer resistance, short circuit current density and efficiency. The graph shows the differences of the means of the short circuit current densities and efficiencies of the solar cell presented in Figure 32 measured before and after degradation. Additionally, single hole transport layers with the three different PANI:PSS ratios were degraded under ambient conditions and illumination for 72 hours, with the resistance measured before and after degradation, which is included as factor of

increase in resistance. A clear coherence can be observed from the measured hole transport layer resistance to the decrease in short circuit current density and power conversion efficiency. The higher the PSS content the lower is the increase in hole transport layer resistance with degradation. Thus, with increasing PSS content the lower is the decrease in short circuit current density and power conversion efficiency.

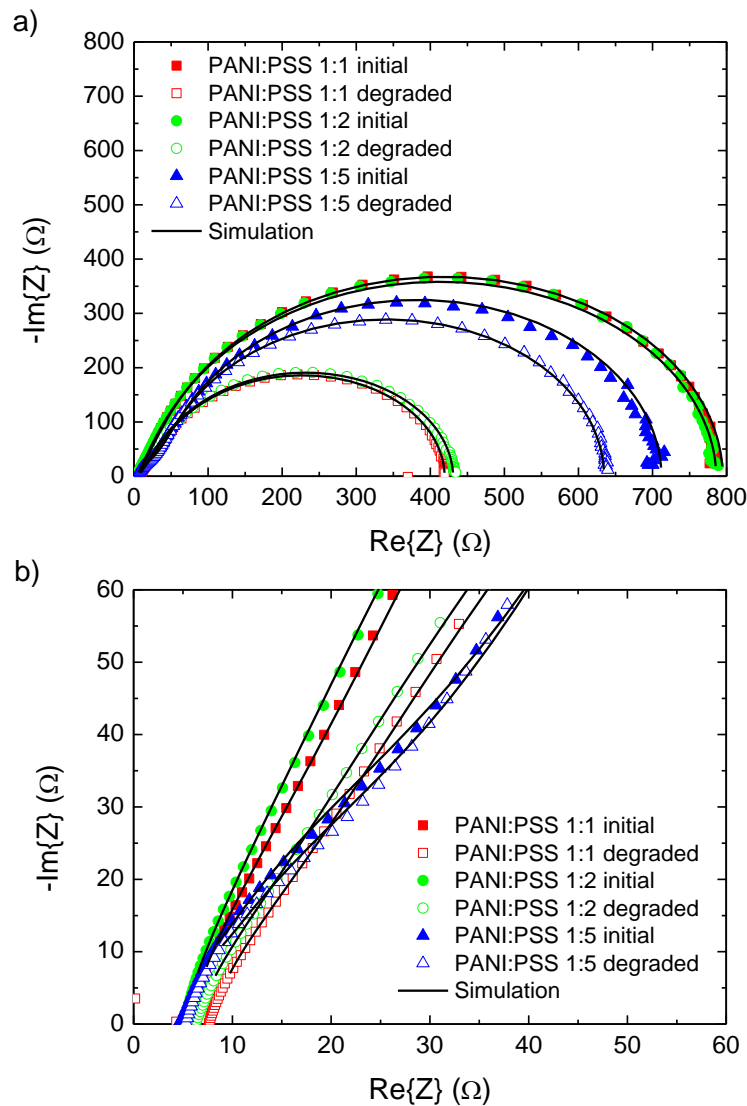


**Figure 33:** a) Cole-Cole plot shown for the frequency range of 1MHz down to 100 Hz and b) zoom in the high frequency range, measured in short circuit conditions under illumination (AM1.5G) with  $100\text{mW cm}^{-2}$ . Lines are simulations according to the equivalent circuit shown in Figure 21.

In order to further investigate the origin of the increased stability of PANI:PSS based hole transport layers with increasing PSS content, Cole-Cole plots, capacitance-frequency and loss-frequency spectra were recorded using impedance spectroscopy, which are shown in Figure 34 and Figure 35, respectively. The Cole-Cole plot, the capacitance and loss spectra were measured under short circuit conditions under illumination of an AM1.5G spectrum with an intensity of  $100 \text{ mW cm}^{-2}$  to determine the correlation between the hole transport layer resistance and the short circuit current density.

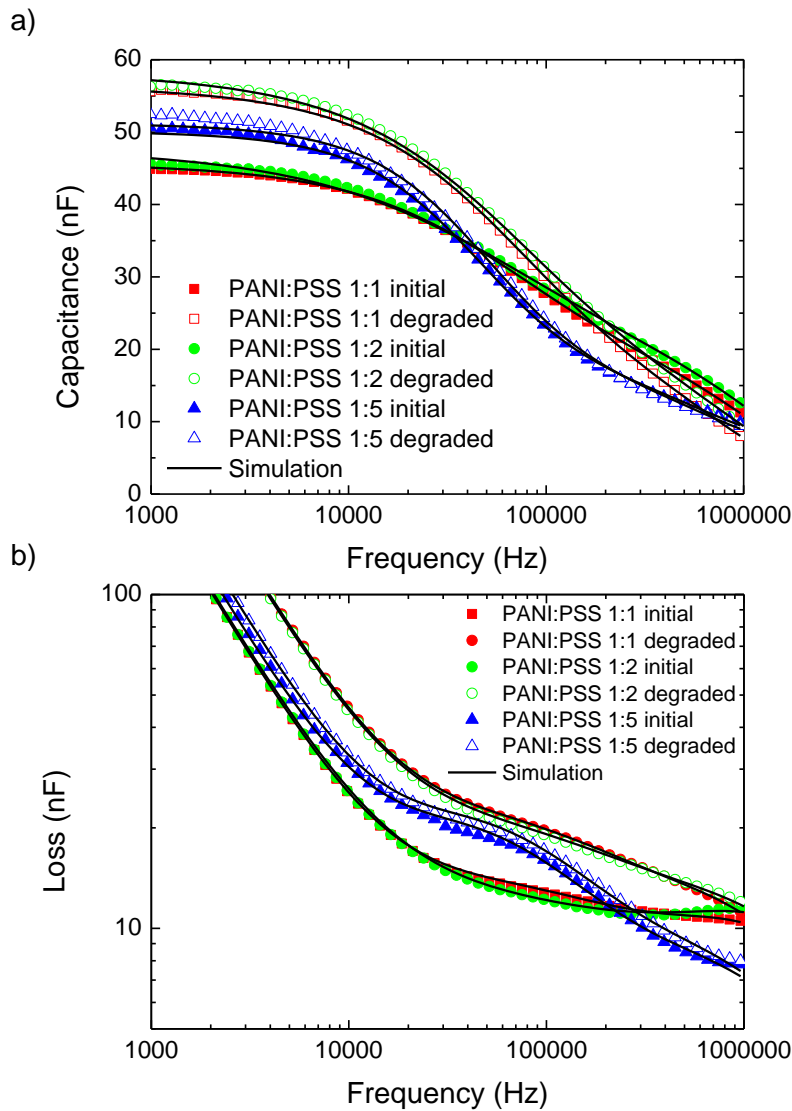


**Figure 34:** a) Capacitance and b) loss spectra of hole transport layers with varying PSS content before and after degradation. Lines are simulations according to the equivalent circuit shown in Figure 21.

In contrast to the increasing resistance with PSS content, the impedance gives a slightly lower value of around 700  $\Omega$  for a ratio of 1:1 and impedances of around 800  $\Omega$  for the hole transport layers with lower PSS content. In addition, the low conductivity of the hole transport layer with a PANI:PSS ratio of 1:1 presents an additional high frequency arc. This is in accordance to the findings in chapter 4.1, where a  $\text{TiO}_x$  interlayer in inverted solar cells initially shows a low conductivity, which also appeared as a high frequency arc in the Cole-Cole plot.

**Table 4: Values used for simulation of curves shown in Figure 34 and Figure 35 using the equivalent circuit shown in Figure 21.**

	$R_s$ ( $\Omega$ )	$R_i$ ( $\Omega$ )	$C_i$ (nF)	$R_b$ ( $\Omega$ )	$C_{geo}$ (nF)	$C_{dis}$ (nF)	$CPE-T_{dis}$ ( $\mu F$ )	$CPE-P_{dis}$
PANI:PSS 1:1 initial	2.8	3.35	4.6	788.5	18.97	27.51	247.84	0.298
PANI:PSS 1:1 degraded	2.8	5.28	3.27	411.2	18.97	39.76	391.72	0.295
PANI:PSS 1:2 initial	2.8	2.47	9.46	780.6	18.45	30.0	78.50	0.386
PANI:PSS 1:2 degraded	2.8	3.84	6.82	424	18.45	41.80	250.47	0.332
PANI:PSS 1:5 initial	2.8	5.42	16.17	703.6	17.4	33.97	1393.9	0.160
PANI:PSS 1:5 degraded	2.8	5.74	13.53	626	17.4	35.29	1504.7	0.164

In order to understand this, one has to take into account the capacitance and loss spectra shown in Figure 35. Around the frequency of 60 kHz a pronounced shoulder of the PANI:PSS with a ratio of 1:5 can be identified in the capacitance spectrum, which is in accordance with the high frequency arc in the Cole-Cole plot and can also being identified as a peak in the loss spectrum also around 60 kHz.

Additionally, the equivalent circuit shown in Figure 21, which was established to investigate the influence of the  $\text{TiO}_x$  interlayer on the formation of s-shaped IV characteristics is used to simulate the impedance data according to the values presented in Table 4 and is shown as lines in Figure 34 and Figure 35. The lead resistance  $R_s$  was fixed at  $2.8 \Omega$  and the geometrical capacitance was extracted from the negative regime of the respective CV curves.

In accordance with chapter 4.1 one can understand the high frequency arc as the formation of a space charge region near the hole transport layer interface. The impedance and capacitance is thus not only defined by the resistance values of the respective layers but also by the internal charge build-up at the hole transport layer interface. However, in this case the conductivity of hole transport layer is not low enough to lead to an s-shaped IV characteristics due to sufficient charge extraction capabilities, which is also reflected by the simulated  $R_i \sim 5 \Omega$  values shown in Table 4, being well below  $124.7 \Omega$  for the  $\text{TiO}_x$  interlayer before light soaking. However, the initially low solar cell performance of the PANI:PSS 1:5 containing solar cell can be ascribed to formation of a space charge.

After degradation, the resistance  $R_b$  representing the active bulk resistance is almost reduced twofold for the hole transport layers containing less PSS, whereas the solar cell with the more stable hole transport layer with a ratio of 1:5 presents only minor changes. More apparently the resistance attributed to the hole transport interlayer  $R_i$  is increasing upon degradation. In detail the increase in  $R_i$  becomes less with increasing PSS content, which is in accordance to the solar cell performance extracted from the IV characteristics. In agreement, the loss spectra reveals the formation of a broad peak for PANI:PSS 1:1 and PANI:PSS 1:2 upon degradation due to the increase in  $R_i$ , whereas the already initially present peak for the PANI:PSS 1:5 is almost unaffected.

From these results, it appears that the PSS induces a stabilizing property. Due to the structural conformation within the hole transport layer, a higher PSS content

results in enrichment of PSS at the interface of the hole transport layer and the active bulk of the solar cell. Therefore, a possible degradation pathway is the oxidation of PANI arising from residual water in encapsulated devices, which can be reduced by the addition of stabilizing PSS.

## 5 Conclusions

This thesis gives insights in the understanding of intrinsic and extrinsic degradation mechanisms using impedance spectroscopy. An inverted solar cell structure for the analysis of s-shaped IV characteristics as well as novel hole transport layer materials are investigated.

In chapter 4.1 inverted P3HT:PCBM based solar cells with a  $\text{TiO}_x$  interlayer between the cathode and active layer are investigated. The device acts a model system in which the shape of the IV characteristics can be reproducibly controlled and switched from s-shaped to regular shaped. The initial IV characteristics demonstrate a strong s-shape which disappears upon light soaking with UV radiation. Impedance spectroscopy and equivalent circuit analysis is used to investigate the solar cell. The resistance of the  $\text{TiO}_x$  interlayer is found to decrease with UV illumination time. This correlates with the transition from s-shaped to regular shaped IV curves. These results suggest that the resistance of the  $\text{TiO}_x$  interlayer has major influence on the shape of the IV characteristics.

Chapter 4.2 presents the results of using different solvents for the hole transport layer formulations. In detail, the influences of PEDOT:PSS ( $\text{H}_2\text{O}$ ), PANI:PSS ( $\text{H}_2\text{O}$ ) or PANI:PSS (IPA) on the device stability are investigated. The stability of the solar cells is observed to be lower in the devices prepared with water based hole transport layers compared to devices prepared using the IPA based hole transport layer, particularly in the case of non-encapsulated devices. In encapsulated devices an increase in the intrinsic stability can be observed for the solar cells prepared with the IPA based hole transport layer. The DOS calculated from impedance spectroscopy measurements shows additional trap states for non-encapsulated water based hole transport layers.

In chapter 4.3 the composition of a water based PANI:PSS hole transport layer with different ratios of PSS to PANI is investigated with regards to solar cell effi-

ciency and stability. Initially, solar cells with lower PSS content show superior performance due to higher conductivity of the hole transport layer. The conductivity of the hole transport layers decreases drastically more upon degradation, if less PSS is present. Devices with high PSS content show lower losses in all solar cell parameters after degradation. Hence, a tradeoff has to be found for the optimal ratio of PANI:PSS for enabling both, high performance and lifetime.

In conclusion, this thesis presents findings on novel interlayers and interfaces adopted in organic solar cells for efficient charge extraction and improving solar cell stability, showing that not only research on active materials and their stability is important, but also variations in hole and electron transport layers have tremendous impact on the device performance and stability of organic solar cells.

## Bibliography

- [1] [http://www.ipcc.ch/pdf/assessment-report/ar4/syr/ar4\\_syr.pdf](http://www.ipcc.ch/pdf/assessment-report/ar4/syr/ar4_syr.pdf), last accessed on 12-17-2011.
- [2] [http://srren.ipcc-wg3.de/report/IPCC\\_SRREN\\_Full\\_Report.pdf](http://srren.ipcc-wg3.de/report/IPCC_SRREN_Full_Report.pdf), last accessed on 12-17-2011.
- [3] M.A. Green, *Third Generation Photovoltaics*, Springer, Berlin **2003**.
- [4] C.J. Brabec, N.S. Sariciftci, J.C. Hummelen, Plastic solar cells, *Advanced Functional Materials* **2001**, *11*, 15-26.
- [5] S. Günes, H. Neugebauer, N.S. Sariciftci, Conjugated polymer-based organic solar cells, *Chemical Reviews* **2007**, *107*, 1324-1338.
- [6] C.J. Brabec, S. Gowrisanker, J.J.M. Halls, D. Laird, S. Jia, S.P. Williams, Polymer-fullerene bulk-heterojunction solar cells, *Advanced Materials* **2010**, *22*, 3839-3856.
- [7] <http://www.konarka.com>, last accessed on 12-17-2011.
- [8] <http://www.heliatek.com>, last accessed on 12-17-2011.
- [9] <http://www.energy-sunbags.de>, last accessed on 12-17-2011.
- [10] Y. Liang, L. Yu, Development of semiconducting polymers for solar energy harvesting, *Polymer Reviews* **2010**, *50*, 454-473.
- [11] A. Facchetti,  $\pi$ -Conjugated polymers for organic electronics and photovoltaic cell applications, *Chemistry of Materials* **2011**, *23*, 733-758.
- [12] J. Hauch, P. Schilinsky, S. Choulis, R. Childers, M. Biele, C.J. Brabec, Flexible organic P3HT:PCBM bulk-heterojunction modules with more than 1 year outdoor lifetime, *Solar Energy Materials and Solar Cells* **2008**, *92*, 727-731.
- [13] F.C. Krebs, K. Norrman, Analysis of the failure mechanism for a stable organic photovoltaic during 10 000 h of testing, *Progress in Photovoltaics: Research and Application* **2007**, *15*, 697-712.
- [14] M. Jørgensen, K. Norrman, F.C. Krebs, Stability/degradation of polymer solar cells, *Solar Energy Materials and Solar Cells* **2008**, *92*, 686-714.

- [15] A. Seemann, H.-J. Egelhaaf, C.J. Brabec, J. Hauch, Influence of oxygen on semi-transparent organic solar cells with gas permeable electrodes, *Organic Electronics* **2009**, *10*, 1424-1428.
- [16] H. Hintz, H.-J. Egelhaaf, L. Lueer, J. Hauch, H. Peisert, T. Chassé, Photodegradation of P3HT—A systematic study of environmental factors *Chemistry of Materials* **2011**, *23*, 145-154.
- [17] K. Norrman, S. Gevorgyan, F.C. Krebs, Water-induced degradation of polymer solar cells studied by H<sub>2</sub><sup>18</sup>O labeling, *ACS Applied Materials & Interfaces* **2009**, *1*, 102-112.
- [18] M. Schwoerer, H.C. Wolf, *Organic Molecular Solids*, Wiley-VCH, Weinheim **2007**.
- [19] A. Pochettino, Sul comportamento foto-elettrico dell' antracene, *Accademia Nazionale dei Lincei* **1906**, *15*, 355-363.
- [20] F. Gutmann, L.E. Lyons, *Organic Semiconductors*, Wiley, New York **1967**.
- [21] R. McNeill, R. Siudak, J.H. Wardlaw, D.E. Weiss, Electronic conduction in polymers I. the chemical structure of polypyrrole, *Australian Journal of Chemistry* **1963**, *16*, 1056-1075.
- [22] B.A. Bolto, D.E. Weiss, Electronic conduction in polymers II. the electrochemical reduction of polypyrrole at controlled potential, *Australian Journal of Chemistry* **1963**, *16*, 1076-1089.
- [23] B.A. Bolto, R. McNeill, D.E. Weiss, Electronic conduction in polymers III. electronic properties of polypyrrole, *Australian Journal of Chemistry* **1963**, *16*, 1090-1103.
- [24] J.E. McGinness, Mobility gaps: a mechanism for band gaps in melanins, *Science* **1972**, *177*, 896-897.
- [25] J. McGinness, P. Corry, P. Proctor, Amorphous semiconductor switching in melanins, *Science* **1974**, *183*, 853-855.
- [26] H. Shirakawa, E.J. Louis, A.G. MacDiarmid, C.K. Chiang, A.J. Heeger, Synthesis of electrically conducting organic polymers: halogen derivatives of polyacetylene, (CH)<sub>x</sub>, *Journal of the Chemical Society, Chemical Communications* **1977**, *16*, 578-580.

- [27] C.K. Chiang, C.R. Fincher Jr., Y.W. Park, A.J. Heeger, H. Shirakawa, E.J. Louis, S.C. Gau, A.G. MacDiarmid, Electrical Conductivity in Doped Polyacetylene, *Physical Review Letters* **1977**, *39*, 1098-1101.
- [28] C.W. Tang, Two-layer organic photovoltaic cell, *Applied Physics Letters* **1986**, *48*, 183-185.
- [29] C.W. Tang, S. VanSlyke, Organic electroluminescent diodes, *Applied Physics Letters* **1987**, *51*, 913-915.
- [30] F.C. Krebs, Fabrication and processing of polymer solar cells: a review of printing and coating techniques, *Solar Energy Materials and Solar Cells* **2009**, *93*, 394-412.
- [31] N.S. Sariciftci, L. Smilowitz, A.J. Heeger, F. Wudl, Photoinduced electron transfer from a conducting polymer to buckminsterfullerene, *Science* **1992**, *258*, 1474-1476.
- [32] A. Miller, E. Abrahams, Impurity conduction at low concentrations, *Physical Review* **1960**, *120*, 745-755.
- [33] A.J. Mozer, G. Dennler, N. Sariciftci, M. Westerling, A. Pivrikas, R. Österbacka, G. Juška, Time-dependent mobility and recombination of the photoinduced charge carriers in conjugated polymer/fullerene bulk heterojunction solar cells, *Physical Review B* **2005**, *72*, 035217.
- [34] H. Bässler, Charge transport in disordered organic photoconductors: a monte carlo simulation study, *Physica Status Solidi (B)* **1993**, *175*, 15-56.
- [35] D. Monroe, Hopping in exponential band tails, *Physical Review Letters* **1985**, *54*, 146-149.
- [36] S. Baranovskii, H. Cordes, F. Hensel, G. Leising, Charge-carrier transport in disordered organic solids, *Physical Review B* **2000**, *62*, 7934-7938.
- [37] S.D. Baranovskii, T. Faber, F. Hensel, P. Thomas, The applicability of the transport-energy concept to various disordered materials, *Journal of Physics: Condensed Matter* **1997**, *9*, 2699-2706.
- [38] D. Hertel, H. Bässler, Photoconduction in amorphous organic solids, *Chemical Physics and Physical Chemistry* **2008**, *9*, 666-688.
- [39] H. Böttger, V. Bryksin, *Hopping Conduction In Solids*, VCH Publishers Inc., Berlin **1985**.

- [40] C.J. Brabec, V. Dyakonov, J. Parisi, N.S. Sariciftci, *Organic Photovoltaics*, Springer, Berlin **2003**.
- [41] A. Haugeneder, M. Neges, C. Kallinger, W. Spirkl, U. Lemmer, J. Feldmann, Exciton diffusion and dissociation in conjugated polymer / fullerene blends and heterostructures, *Physical Review B* **1999**, *59*, 346-351.
- [42] D.E. Markov, E. Amsterdam, P.W.M. Blom, A.B. Sieval, J.C. Hummelen, Accurate measurement of the exciton diffusion length in a conjugated polymer using a heterostructure with a side-chain cross-linked fullerene layer, *The Journal of Physical Chemistry. A* **2005**, *109*, 5266-5274.
- [43] P.E. Shaw, A. Ruseckas, I.D.W. Samuel, Exciton diffusion measurements in poly(3-hexylthiophene), *Advanced Materials* **2008**, *20*, 3516-3520.
- [44] J. Parisi, V. Dyakonov, M. Pientka, I. Riedel, C. Deibel, C.J. Brabec, N.S. Sariciftci, Charge transfer and transport in polymer-fullerene solar cells, *Zeitschrift für Naturforschung* **2002**, *57a*, 995-1000.
- [45] S. Braun, W.R. Salaneck, M. Fahlman, Energy-level alignment at organic/metal and organic/organic Interfaces, *Advanced Materials* **2009**, *21*, 1450-1472.
- [46] G. Yu, J. Gao, J.C. Hummelen, F. Wudl, A.J. Heeger, Polymer photovoltaic cells: enhanced efficiencies via a network of internal donor-acceptor heterojunctions, *Science* **1995**, *270*, 1789-1791.
- [47] C. Groves, L.J. a. Koster, N.C. Greenham, The effect of morphology upon mobility: implications for bulk heterojunction solar cells with nonuniform blend morphology, *Journal of Applied Physics* **2009**, *105*, 094510.
- [48] B.M. Hallermann, I. Kriegel, E. Da Como, J.M. Berger, E. von Hauff, J. Feldmann, Charge transfer excitons in polymer/fullerene blends: the role of morphology and polymer chain conformation, *Advanced Functional Materials* **2009**, *19*, 3662-3668.
- [49] M.-S. Kim, J.-S. Kim, J.C. Cho, M. Shtein, L.J. Guo, J. Kim, Flexible conjugated polymer photovoltaic cells with controlled heterojunctions fabricated using nanoimprint lithography, *Applied Physics Letters* **2007**, *90*, 123113.
- [50] J.H. Lee, D.W. Kim, H. Jang, J.K. Choi, J. Geng, J.W. Jung, S.C. Yoon, H.-T. Jung, Enhanced solar-cell efficiency in bulk-heterojunction polymer systems obtained by nanoimprinting with commercially available AAO membrane filters, *Small* **2009**, *5*, 2139-2143.

- [51] Y. Liang, Z. Xu, J. Xia, S.-T. Tsai, Y. Wu, G. Li, C. Ray, L. Yu, For the bright future: bulk heterojunction polymer solar cells with power conversion efficiency of 7.4%, *Advanced Materials* **2010**, *22*, 135-138.
- [52] J.Y. Park, N.R. Hendricks, K.R. Carter, Solvent-assisted soft nanoimprint lithography for structured bilayer heterojunction organic solar cells, *Langmuir* **2011**, *27*, 11251-11258.
- [53] H. Ma, H.-L. Yip, F. Huang, A.K.-Y. Jen, Interface engineering for organic electronics, *Advanced Functional Materials* **2010**, *20*, 1371-1388.
- [54] R. Steim, F.R. Kogler, C.J. Brabec, Interface materials for organic solar cells, *Journal of Materials Chemistry* **2010**, *20*, 2499-2512.
- [55] C.J. Brabec, S.E. Shaheen, C. Winder, N.S. Sariciftci, P. Denk, Effect of LiF/metal electrodes on the performance of plastic solar cells, *Applied Physics Letters* **2002**, *80*, 1288-1290.
- [56] B. Ecker, J.C. Nolasco, J. Pallarés, L.F. Marsal, J. Posdorfer, J. Parisi, E. von Hauff, Degradation effects related to the hole transport layer in organic solar cells, *Advanced Functional Materials* **2011**, *21*, 2705-2711.
- [57] A. Goetzberger, J. Knobloch, B. Voß, *Crystalline Silicon Solar Cells*, Wiley, New York **1998**.
- [58] G. Dennler, C. Lungenschmied, H. Neugebauer, N.S. Sariciftci, M. Latrèche, G. Czeremuszkin, M.R. Wertheimer, A new encapsulation solution for flexible organic solar cells, *Thin Solid Films* **2006**, *511-512*, 349-353.
- [59] C. Lungenschmied, G. Dennler, H. Neugebauer, S.N. Sariciftci, M. Glatthaar, T. Meyer, A. Meyer, Flexible, long-lived, large-area, organic solar cells, *Solar Energy Materials and Solar Cells* **2007**, *91*, 379-384.
- [60] W. Ma, C. Yang, X. Gong, K. Lee, a. J. Heeger, Thermally stable, efficient polymer solar cells with nanoscale control of the interpenetrating network morphology, *Advanced Functional Materials* **2005**, *15*, 1617-1622.
- [61] S. Chambon, A. Rivaton, J.-L. Gardette, M. Firon, Photo- and thermo-oxidation of poly(p-phenylene-vinylene) and phenylene-vinylene oligomer, *Polymer Degradation and Stability* **2011**, *96*, 1149-1158.
- [62] M.O. Reese, A.J. Morfa, M.S. White, N. Kopidakis, S.E. Shaheen, G. Rumbles, D.S. Ginley, Pathways for the degradation of organic photovolta-

- ic P3HT:PCBM based devices, *Solar Energy Materials and Solar Cells* **2008**, *92*, 746-752.
- [63] M.O. Reese, A.M. Nardes, B.L. Rupert, R.E. Larsen, D.C. Olson, M.T. Lloyd, S.E. Shaheen, D.S. Ginley, G. Rumbles, N. Kopidakis, Photoinduced degradation of polymer and polymer-fullerene active layers: experiment and theory, *Advanced Functional Materials* **2010**, *20*, 3476-3483.
- [64] E. Barsoukov, J.R. Macdonald, *Impedance Spectroscopy - Theory, Experiment, And Applications*, Wiley, Hoboken **2005**.
- [65] K.S. Cole, R.H. Cole, Dispersion and absorption in dielectrics I. alternating current characteristics, *The Journal of Chemical Physics* **1941**, *9*, 341-351.
- [66] M.E. Orazem, B. Tribollet, *Electrochemical Impedance Spectroscopy*, Wiley, Hoboken, **2008**.
- [67] C.-C. Chen, B.-C. Huang, M.-S. Lin, Y.-J. Lu, T.-Y. Cho, C.-H. Chang, K.-C. Tien, S.-H. Liu, T.-H. Ke, C.-C. Wu, Impedance spectroscopy and equivalent circuits of conductively doped organic hole-transport materials, *Organic Electronics* **2010**, *11*, 1901-1908.
- [68] H.C.F. Martens, H.B. Brom, P.W.M. Blom, Frequency-dependent electrical response of holes in poly(p-phenylene vinylene), *Physical Review B* **1999**, *60*, 8489-8492.
- [69] S. Berleb, W. Brütting, Dispersive Electron Transport in tris(8-hydroxyquinoline) aluminum (Alq<sub>3</sub>) probed by impedance spectroscopy, *Physical Review Letters* **2002**, *89*, 286601.
- [70] S.H. Park, A. Roy, S. Beaupré, S. Cho, N. Coates, J.S. Moon, D. Moses, M. Leclerc, K. Lee, A.J. Heeger, Bulk heterojunction solar cells with internal quantum efficiency approaching 100%, *Nature Photonics* **2009**, *3*, 297-302.
- [71] I. Eisgruber, Blue-photon modification of nonstandard diode barrier in CuInSe<sub>2</sub> solar cells, *Solar Energy Materials and Solar Cells* **1998**, *53*, 367-377.
- [72] M. Glatthaar, M. Riede, N. Keegan, K. Sylvesterhvid, B. Zimmermann, M. Niggemann, A. Hinsch, A. Gombert, Efficiency limiting factors of organic bulk heterojunction solar cells identified by electrical impedance spectroscopy, *Solar Energy Materials and Solar Cells* **2007**, *91*, 390-393.

- [73] A. Wagenpfahl, D. Rauh, M. Binder, C. Deibel, V. Dyakonov, S-shaped current-voltage characteristics of organic solar devices, *Physical Review B* **2010**, *82*, 115306.
- [74] J.C. Wang, X.C. Ren, S.Q. Shi, C.W. Leung, P.K.L. Chan, Charge accumulation induced s-shape J-V curves in bilayer heterojunction organic solar cells, *Organic Electronics* **2011**, *12*, 880-885.
- [75] W. Tress, A. Petrich, M. Hummert, M. Hein, K. Leo, M. Riede, Imbalanced mobilities causing s-shaped IV curves in planar heterojunction organic solar cells, *Applied Physics Letters* **2011**, *98*, 063301.
- [76] W. Tress, K. Leo, M. Riede, Influence of hole-transport layers and donor materials on open-circuit voltage and shape of I-V curves of organic solar cells, *Advanced Functional Materials* **2011**, *21*, 2140-2149.
- [77] R. Steim, S. Choulis, P. Schilinsky, C.J. Brabec, Interface modification for highly efficient organic photovoltaics, *Applied Physics Letters* **2008**, *92*, 093303.
- [78] J.Y. Kim, S.H. Kim, H.-H. Lee, K. Lee, W. Ma, X. Gong, A.J. Heeger, New architecture for high-efficiency polymer photovoltaic cells using solution-based titanium oxide as an optical spacer, *Advanced Materials* **2006**, *18*, 572-576.
- [79] A.K. Jonscher, Dielectric relaxation in solids, *Journal of Physics D: Applied Physics* **1999**, *32*, 57-70.
- [80] J. Nelson, A.M. Eppler, I.M. Ballard, Photoconductivity and charge trapping in porous nanocrystalline titanium dioxide, *Journal of Photochemistry and Photobiology A: Chemistry* **2002**, *148*, 25-31.
- [81] C. Tao, S. Ruan, G. Xie, X. Kong, L. Shen, F. Meng, C. Liu, X. Zhang, W. Dong, W. Chen, Role of tungsten oxide in inverted polymer solar cells, *Applied Physics Letters* **2009**, *94*, 043311.
- [82] V. Shrotriya, G. Li, Y. Yao, C.-W. Chu, Y. Yang, Transition metal oxides as the buffer layer for polymer photovoltaic cells, *Applied Physics Letters* **2006**, *88*, 073508.
- [83] R. Jin, P. Levermore, J. Huang, X. Wang, D.D.C. Bradley, J.C. deMello, On the use and influence of electron-blocking interlayers in polymer light-emitting diodes, *Physical Chemistry Chemical Physics* **2009**, *11*, 3455-3462.

- [84] G. Gustafsson, Y. Cao, G. M. Treacy, F. Klavetter, Flexible light-emitting diodes made from soluble conducting polymers, *Nature* **1992**, 357, 477-479.
- [85] H. Bejbouj, L. Vignau, J.L. Miane, T. Olinga, G. Wantz, A. Mouhsen, E.M. Oualim, M. Harmouchi, Influence of the nature of polyaniline-based hole-injecting layer on polymer light emitting diode performances, *Materials Science and Engineering: B* **2010**, 166, 185-189.
- [86] H. Bejbouji, L. Vignau, J.L. Miane, M.-T. Dang, E.M. Oualim, M. Harmouchi, A. Mouhsen, Polyaniline as a hole injection layer on organic photovoltaic cells, *Solar Energy Materials and Solar Cells* **2010**, 94, 176-181.
- [87] M.P.D. Jong, L.J.V. Ijzendoorn, M.J.A.D. Voigt, Stability of the interface between indium-tin-oxide in polymer light-emitting diodes, *Applied Physics Letters* **2000**, 77, 2255-2257.
- [88] K. Kawano, R. Pacios, D. Poplavskyy, J. Nelson, D. Bradley, J. Durrant, Degradation of organic solar cells due to air exposure, *Solar Energy Materials and Solar Cells* **2006**, 90, 3520-3530.
- [89] B. Zimmermann, U. Würfel, M. Niggemann, Longterm stability of efficient inverted P3HT:PCBM solar cells, *Solar Energy Materials and Solar Cells* **2009**, 93, 491-496.
- [90] S.K. Hau, H.-L. Yip, N.S. Baek, J. Zou, K. O'Malley, A.K.-Y. Jen, Air-stable inverted flexible polymer solar cells using zinc oxide nanoparticles as an electron selective layer, *Applied Physics Letters* **2008**, 92, 253301.
- [91] M.T. Lloyd, D.C. Olson, P. Lu, E. Fang, D.L. Moore, M.S. White, M.O. Reese, D.S. Ginley, J.W.P. Hsu, Impact of contact evolution on the shelf life of organic solar cells, *Journal of Materials Chemistry* **2009**, 19, 7638-7642.
- [92] K. Norrman, M.V. Madsen, S. a Gevorgyan, F.C. Krebs, Degradation patterns in water and oxygen of an inverted polymer solar cell, *Journal of the American Chemical Society* **2010**, 132, 16883-16892.
- [93] I. Riedel, J. Parisi, V. Dyakonov, L. Lutsen, D. Vanderzande, J.C. Hummelen, Effect of temperature and illumination on the electrical characteristics of polymer–fullerene bulk-heterojunction solar cells, *Advanced Functional Materials* **2004**, 14, 38-44.

- [94] L.J.A. Koster, V.D. Mihailetschi, H. Xie, P.W.M. Blom, Origin of the light intensity dependence of the short-circuit current of polymer/fullerene solar cells, *Applied Physics Letters* **2005**, *87*, 203502.
- [95] L.J.A. Koster, V.D. Mihailetschi, R. Ramaker, P.W.M. Blom, Light intensity dependence of open-circuit voltage of polymer:fullerene solar cells, *Applied Physics Letters* **2005**, *86*, 123509.
- [96] T. Walter, R. Herberholz, C. Müller, H.W. Schock, Determination of defect distributions from admittance measurements and application to Cu(In,Ga)Se<sub>2</sub> based heterojunctions, *Journal of Applied Physics* **1996**, *80*, 4411-4420.
- [97] K.L. Chopra, S.R. Das, *Thin Film Solar Cells*, Plenum, New York **1983**.
- [98] J.C. Nolasco, A. Sánchez-Díaz, R. Cabré, J. Ferré-Borrull, L.F. Marsal, E. Palomares, J. Pallarès, Relation between the barrier interface and the built-in potential in pentacene/C<sub>60</sub> solar cell, *Applied Physics Letters* **2010**, *97*, 013305.
- [99] S.M. Sze, K.K. Ng, *Physics of Semiconductor Devices*, Wiley, New York **2007**.
- [100] I. Torres, D.M. Taylor, E. Itoh, Interface states and depletion-induced threshold voltage instability in organic metal-insulator-semiconductor structures, *Applied Physics Letters* **2004**, *85*, 314-316.
- [101] A. Liu, S. Zhao, S.-B. Rim, J. Wu, M. Könnemann, P. Erk, P. Peumans, Control of electric field strength and orientation at the donor-acceptor interface in organic solar cells, *Advanced Materials* **2008**, *20*, 1065-1070.
- [102] H. Hintz, H.-J. Egelhaaf, H. Peisert, T. Chassé, Photo-oxidation and ozonization of poly(3-hexylthiophene) thin films as studied by UV/VIS and photoelectron spectroscopy, *Polymer Degradation and Stability* **2010**, *95*, 818-825.
- [103] F.T. Reis, L.F. Santos, R.F. Bianchi, H.N. Cunha, D. Mencaraglia, R.M. Faria, Application of abrupt cut-off models in the analysis of the capacitance spectra of conjugated polymer devices, *Applied Physics A* **2009**, *96*, 909-914.
- [104] P.P. Boix, G. Garcia-Belmonte, U. Muñecas, M. Neophytou, C. Waldauf, R. Pacios, Determination of gap defect states in organic bulk heterojunction solar cells from capacitance measurements, *Applied Physics Letters* **2009**, *95*, 233302.

- [105] O.D. Jurchescu, B.H. Hamadani, H.D. Xiong, S.K. Park, S. Subramanian, N.M. Zimmerman, J.E. Anthony, T.N. Jackson, D.J. Gundlach, Correlation between microstructure, electronic properties and flicker noise in organic thin film transistors, *Applied Physics Letters* **2008**, 92, 132103.

## Publications and conference contributions

### Publications:

Degradation effects related to the hole transport layer in organic solar cells; Bernhard Ecker, Jairo C. Nolasco, Josep Pallarés, Lluís F. Marsal, Jörg Posdorfer, Jürgen Parisi, and Elizabeth von Hauff, *Adv. Funct. Mater.* (2011) **21**, 2705-2711.

The influence of molecular weight on the short channel effect in polymer based field effect transistors; Ali V. Tunc, Bernhard Ecker, Zekeriya Dogruyol, Sabrina Jüchter, Ahmet L. Ugur, Ali Erdogmus, Sait E. San, Jürgen Parisi, and Elizabeth von Hauff, *J. Polym. Sci., Part B: Polym. Phys.* (2011), **50**, 117-124.

Investigations of Material Parameters and Device Stability in Polymer:Fullerene Solar Cells Using Impedance Spectroscopy; Bernhard Ecker, Jürgen Parisi, and Elizabeth von Hauff, *Proc. 26th EU PVSEC, Hamburg* (2011), 595 DOI: 10.4229/26thEUPVSEC2011-1DV.3.43.

Influence of different copolymer sequences in low band gap polymers on their performance in organic solar cells; Alexander Lange, Hartmut Krüger, Bernhard Ecker, Ali Veysel Tunc, Elizabeth von Hauff, and Mauro Morana, *J. Polym. Sci., Part A: Polym. Chem.* (2012), **50**, 1622–1635.

Understanding S-Shaped Current–Voltage Characteristics in Organic Solar Cells Containing a TiO<sub>x</sub> Interlayer with Impedance Spectroscopy and Equivalent Circuit Analysis; Bernhard Ecker, Hans-Joachim Egelhaaf, Roland Steim, Jürgen Parisi, and Elizabeth von Hauff, *J. Phys. Chem. C* (2012) DOI: 10.1021/jp305206d.

### **Conference contributions:**

From organic single carrier diodes to bulk heterojunction solar cells: an electrical characterization by impedance spectroscopy; Bernhard Ecker, Elizabeth von Hauff, and Jürgen Parisi; DPG Frühjahrstagung 21.03.2010 - 26.03.2010; Regensburg, Germany; poster.

Impedance spectroscopy on organic semiconducting materials for application in photovoltaics; Bernhard Ecker, Elizabeth von Hauff, and Jürgen Parisi; 4th PhD spring workshop: Organic materials for flexible devices; 19.04.2010 – 20.04.2010; University of southern Denmark, Sonderburg, Denmark; poster.

Comparing organic single-carrier-diodes to bulk-heterojunctions using impedance spectroscopy; Bernhard Ecker, Elizabeth von Hauff, and Jürgen Parisi; CIMTEC 2010; 13.06.2010 – 18.06.2010, Montecatini Terme, Italy; poster.

Investigations of different hole transport layers in polymer:fullerene solar cells; Bernhard Ecker, Jörg Posdorfer, Elizabeth von Hauff, and Jürgen Parisi; ICSM 2010; 04.07.2010 – 09.07.2010; Kyoto, Japan; poster.

Degradation effects related to the hole transport layer in organic solar cells; Bernhard Ecker, Jairo C. Nolasco, Josep Pallarés, Lluís F. Marsal, Jörg Posdorfer, Jürgen Parisi, and Elizabeth von Hauff; DPG Frühjahrstagung, 13.03.2011 – 18.03.2011, Dresden, Germany; talk.

Degradation effects related to the hole transport layer in organic solar cells; Bernhard Ecker, Jairo C. Nolasco, Josep Pallarés, Lluís F. Marsal, Jörg Posdorfer, Jürgen Parisi, and Elizabeth von Hauff; E-MRS spring meeting, 9.05.2011 – 13.05.2011, Nice, France; poster.

Novel materials for improved stability in organic solar cells; Bernhard Ecker, Jairo C. Nolasco, Josep Pallarés, Lluís F. Marsal, Jörg Posdorfer, Jürgen Parisi,

and Elizabeth von Hauff; EUPVSEC, 5.9.2011-9.9.2011, Hamburg, Germany,  
poster.

Intrinsic and Extrinsic Material Instabilities in Polymer:Fullerene Bulk  
Heterojunction Solar Cells; Elizabeth von Hauff, Bernhard Ecker, Antonietta De  
Sio and Jürgen Parisi, MRS fall meeting, 28.11.2011 – 2.12.2011, Boston, USA,  
talk.

## Acknowledgements

First of all I would like to thank Jürgen Parisi for giving me the possibility to pursue my work in his excellent group and taking care for making available the best equipment. I also would like to thank him for the many given possibilities to visit all the conferences, sharing insights into the scientific world and being interested in my work and adding to it.

I am also very grateful for having Elizabeth von Hauff as my supervisor. Thanks to her keen sense of science as well as her ability to create a highly motivating atmosphere it was almost always fun working towards a PhD.

I also have to thank Carsten Agert and Achim Kittel for showing interest in my work, writing certificates and taking their time for my defense.

I also would like to thank all the members of the group “Energie- und Halbleiterforschung”. Especially, I would like to mention Antonietta De Sio, Janet Neerken, Thomas Madena, Ali Tunc, Robin Knecht, Nikolay Radychev, Jörg Ohland, Martin Knipper, Ludwig Worbes, Hans Holtorf, Wilhelm Jürgens, Matthias Macke, Folker Zutz (also for the help with XRD measurements), Christine Chory and Björn Kempken (both for advises regarding the  $\text{TiO}_x$  synthesis).

Jörg Posdorfer is acknowledged for his collaborative way, sharing insights to electrochemistry and for all the materials he provided.

Jairo C. Nolasco, Josep Pallarés and Lluís F. Marsal are acknowledged for the very enjoyable and effective way of collaborating.

I would also like to thank Hans-Joachim Egelhaaf and Christoph Lungenschmied for many discussions on impedance spectroscopy during project meetings and telephone conferences, as well as for inviting me to Linz for doing measurements together.

Many thanks go to Alex Lange und Hartmut Krüger for having a great time in Kyoto and the resulting collaboration.

The Helmholtz Zentrum Berlin (HZB) is acknowledged for making available AFORSHET 2.2 for free.

Finally, I would like to thank the Federal Ministry of Education and Research (BMBF) and the university society Oldenburg (UGO) for financial support.

## **Curriculum vitae**

### **Persönliche Daten:**

Name: Bernhard Ecker

Geburtsdatum: 3. August 1983

Geburtsort: Landshut

### **Wissenschaftliche Anstellung:**

Seit 02/2012      Wissenschaftlicher Angestellter an der Universität Freiburg in  
der Arbeitsgruppe von Prof. Dr. Elizabeth von Hauff

02/2009–            Wissenschaftlicher Angestellter an der Universität Oldenburg in  
02/2012            der Abteilung für Energie- und Halbleiterforschung (Prof. Dr.  
Jürgen Parisi)

### **Studium:**

06.02.2009        Abschluss des Master-Studiums mit dem Erhalt des  
akademischen Grades „Master of Science“ (Note 1,83)

05/2008 –        Universität Augsburg, Lehrstuhl für Experimentalphysik IV  
02/2009            Anfertigung der Masterarbeit: „Strukturelle, morphologische  
und photoelektrische Charakterisierung organischer Donor-  
Akzeptor Solarzellen“ (Betreuer: Prof. Dr. Wolfgang Brütting)

04/2007 –        Universität Augsburg  
02/2009            Master-Studiengang Materials Science

19.12.2006        Abschluss des Bachelor-Studiums mit dem Erhalt des  
akademischen Grades „Bachelor of Science“ (Note 2,24)

05/2006 – Universität Augsburg, Lehrstuhl für Experimentalphysik IV  
12/2006 Anfertigung der Bachelorarbeit: „Anodische Oxidation von Aluminium zur Herstellung von Gate-Isolatoren für organische Feldeffektbauelemente“ (Betreuer: Prof. Dr. Wolfgang Brütting)  
10/2003 – Universität Augsburg  
12/2006 Bachelor-Studiengang Materialwissenschaften

### **Schulbildung**

27.06.2003 Maristen-Gymnasium, Furth bei Landshut  
Abschluss: Allgemeine Hochschulreife (Note 2,5)

## **Erklärung**

Hiermit erkläre ich, dass ich diese Arbeit selbstständig verfasst und nur die angegebenen Hilfsmittel benutzt habe.

Oldenburg, den 3.02.2012

.....

**Bernhard Ecker**